



HAL
open science

ÆSOPUS 2.1: Low-temperature Opacities Extended to High Pressure

Paola Marigo, Francesco Addari, Diego Bossini, Alessandro Bressan, Guglielmo Costa, Léo Girardi, Giada Pastorelli, Michele Trabucchi, Guglielmo Volpato

► **To cite this version:**

Paola Marigo, Francesco Addari, Diego Bossini, Alessandro Bressan, Guglielmo Costa, et al.. ÆSOPUS 2.1: Low-temperature Opacities Extended to High Pressure. *The Astrophysical Journal*, 2024, 976, 10.3847/1538-4357/ad7b27 . insu-04838839

HAL Id: insu-04838839

<https://insu.hal.science/insu-04838839v1>

Submitted on 15 Dec 2024

HAL is a multi-disciplinary open access archive for the deposit and dissemination of scientific research documents, whether they are published or not. The documents may come from teaching and research institutions in France or abroad, or from public or private research centers.




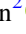



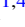
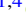
L'archive ouverte pluridisciplinaire **HAL**, est destinée au dépôt et à la diffusion de documents scientifiques de niveau recherche, publiés ou non, émanant des établissements d'enseignement et de recherche français ou étrangers, des laboratoires publics ou privés.



Distributed under a Creative Commons Attribution 4.0 International License



ÆSOPUS 2.1: Low-temperature Opacities Extended to High Pressure

Paola Marigo^{1,5} , Francesco Addari² , Diego Bossini¹ , Alessandro Bressan² , Guglielmo Costa^{3,4} , Léo Girardi⁴ ,
Giada Pastorelli¹ , Michele Trabucchi^{1,4} , and Guglielmo Volpato^{1,4} 

¹ Department of Physics and Astronomy G. Galilei, University of Padova, Vicolo dell'Osservatorio 3, I-35122, Padova, Italy; diego.bossini@unipd.it

² Scuola Internazionale Superiore di Studi Avanzati, Via Bonomea, 265, I-34136, Trieste, Italy

³ Univ Lyon, Univ Lyon1, Ens de Lyon, CNRS, Centre de Recherche Astrophysique de Lyon UMR5574, F-69230 Saint-Genis-Laval, France

⁴ INAF-Osservatorio Astronomico di Padova, Vicolo dell'Osservatorio 5, I-35122, Padova, Italy

Received 2024 May 15; revised 2024 August 29; accepted 2024 September 14; published 2024 November 12

Abstract

We address the critical need for accurate Rosseland mean gas opacities in high-pressure environments, spanning temperatures from 100 K to 32,000 K. Current opacity tables from Wichita State University and ÆSOPUS 2.0 are limited to $\log(R) \leq 1$, where $R = \rho T_6^{-3}$ in units of $\text{g cm}^{-3} (10^6 \text{K})^{-3}$. This is insufficient for modeling very low-mass stars, brown dwarfs, and planets with atmospheres exhibiting higher densities and pressures ($\log(R) > 1$). Leveraging extensive databases such as EXOMOL, EXOMOLOP, MOLLIST, and HITEMP, we focus on expanding the ÆSOPUS opacity calculations to cover a broad range of pressure and density conditions ($-8 \leq \log(R) \leq +6$). We incorporate the thermal Doppler mechanism and microturbulence velocity. Pressure-broadening effects on molecular transitions, leading to Lorentzian or Voigt profiles, are explored in the context of atmospheric profiles for exoplanets, brown dwarfs, and low-mass stars. We also delve into the impact of electron degeneracy and nonideal effects, such as ionization potential depression under high-density conditions, emphasizing its notable influence on Rosseland mean opacities at temperatures exceeding 10,000 K. As a result, this study expands the ÆSOPUS public web interface for customized gas chemical mixtures, promoting flexibility in opacity calculations based on specific research needs. Additionally, precomputed opacity tables, inclusive of condensates, are provided. We present a preliminary application to evolutionary models for very low-mass stars.

Unified Astronomy Thesaurus concepts: [Stellar atmospheric opacity \(1585\)](#); [Astrochemistry \(75\)](#); [Low mass stars \(2050\)](#); [Brown dwarfs \(185\)](#); [Exoplanets \(498\)](#); [Collisional broadening \(2083\)](#)

1. Introduction

Thanks to extensive databases such as EXOMOL (J. Tennyson & S. N. Yurchenko 2012; J. Tennyson et al. 2016), EXOMOLOP (K. L. Chubb et al. 2021), MOLLIST (P. F. Bernath 2020) and HITEMP (L. S. Rothman et al. 2010), we can now rely on the availability of a substantial amount of molecular line list data, which is a significant asset for modeling the atmospheres of hot exoplanets, as well as cool stellar and substellar atmospheres.

Rosseland mean opacities are critical components in modeling stars and substellar objects. To our knowledge, the most widely distributed suppliers of Rosseland mean opacities for $T \lesssim 10,000$ K are the Wichita State University group (D. R. Alexander 1975; D. R. Alexander & J. W. Ferguson 1994; J. W. Ferguson et al. 2005), and the ÆSOPUS team (P. Marigo & B. Aringer 2009; P. Marigo et al. 2022). Two standard variables are used to build Rosseland mean opacity tables:

$$T \text{ and } R = \rho T_6^{-3}, \quad (1)$$

where T is the temperature (in Kelvin) and the R parameter (in $\text{g cm}^{-3} (10^6 \text{K})^{-3}$) includes both the temperature ($T_6 = T/(10^6 \text{K})$), and the gas mass density ρ (in g cm^{-3}). The fact

⁵ This manuscript represents the final work of Prof. Paola Marigo, who passed away before its publication. As her group, we would like to express our deepest gratitude for her guidance, and our commitment to carry forward her legacy.

that smooth opacity interpolations are feasible is the primary motivation behind the selection of these two parameters.

So far, low-temperature opacities have been computed encompassing the range $-8 \leq \log(R) \leq +1$ (J. W. Ferguson et al. 2005; P. Marigo et al. 2022). This range, however, is insufficiently broad to cover the structural characteristics of very low-mass stars, brown dwarfs, and planets (see Section 2). In fact, these objects have atmospheres with high density and pressure, so $\log(R)$ can easily exceed 1. Very low-mass stars ($0.08 \lesssim M/M_\odot \lesssim 0.6$) and substellar objects ($10^{-3} \lesssim M/M_J \lesssim 13$ for exoplanets, $13 \lesssim M/M_J \lesssim 90$ for brown dwarfs, with $M_J \equiv 1$ Jupiter mass) have atmospheres that typically cover temperature ranges of $100 \lesssim T/\text{K} \lesssim 3500$ and gas pressure ranges of $10^{-4} \lesssim P_{\text{gas}}/\text{bar} \lesssim 10^3$ (A. Burrows et al. 2001; D. S. Spiegel et al. 2011; P. A. Wilson et al. 2016; G. D. Mulders et al. 2021). This demonstrates the need of extending the Rosseland mean opacity tables at higher densities and pressures (with $\log(R) > 1$).

The thermal Doppler mechanism is used by both the Wichita State University and ÆSOPUS teams for molecular line broadening. Microturbulence velocity is also included in ÆSOPUS. As we will see in Section 3.2, this approximation is mostly valid over the standard range $-8 \leq \log(R) \leq +1$, but it becomes inadequate when higher R values, hence larger densities and pressures are considered. When moving into the high-density regime, pressure effects broaden molecular transitions, resulting in either Lorentzian or Voigt profiles (A. Burrows et al. 2001; C. M. Sharp & A. Burrows 2007). Figure 1 depicts the pressure–temperature atmospheric profiles of two exoplanets, one brown dwarf, and very low-mass stars. Pressure broadening of spectral molecular lines affects all of

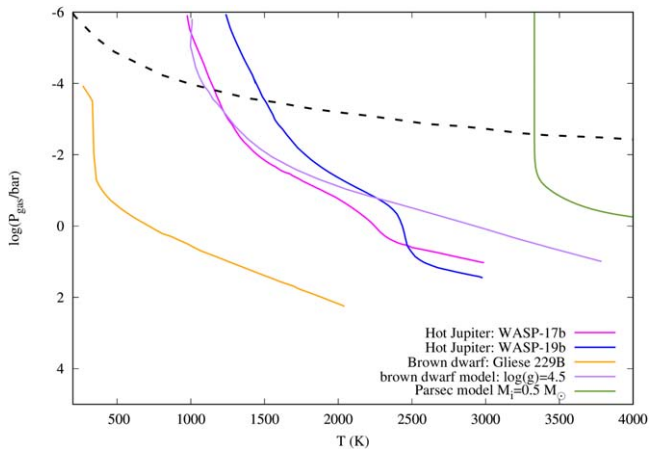


Figure 1. Atmospheric pressure–temperature profiles for exoplanets, brown dwarfs, and very low-mass stars. The two hot Jupiter exoplanets, WASP-17b with a mass of $0.51 M_J$, and WASP-19b with a mass of $1.14 M_J$, were analyzed by D. K. Sing et al. (2016) through Hubble Space Telescope/Spitzer observations. E. Calamari et al. (2022) used an atmospheric retrieval analysis to derive the profile for the brown dwarf Gliese 229B with an estimated mass of $50 M_J$. We also add two theoretical profiles for brown dwarfs with a surface gravity of $\log(g) = 4.5$ (I. Baraffe et al. 2002), and a very low-mass star model from PARSEC (A. Bressan et al. 2012). The dashed black line denotes the limit below which pressure broadening for molecular spectral lines should be included. Refer to Section 3.2 for more details.

these objects’ atmospheres (below the dashed black line). Few works in the past literature, to our knowledge, computed Rosseland mean gas opacities at high densities, namely R. L. Kurucz (1993), R. S. Freedman et al. (2008), M. G. Mal’ugin et al. (2014), R. S. Freedman et al. (2014), adopting scaled solar abundances according to N. Grevesse & A. J. Sauval (1998) or K. Lodders (2003). For zero-metallicity gas, we also refer to the work of P. Lenzuni et al. (1991).

Under high-density conditions, additional important phenomena, namely electron degeneracy and Coulomb interactions between charged particles, must be accounted for in the equation of state (J. Cox & R. Giuli 1968; J. P. Hansen & P. Vieillefosse 1976; A. Y. Potekhin et al. 2009). Furthermore, all charges present in a radiating gas, electrons, and ions, contribute to reducing the energy required to free an electron in the fundamental state. This process is designated as ionization potential depression (IPD; G. Ecker & W. Kröll 1963; J. C. Stewart & K. D. J. Pyatt 1966). We will show that the IPD effect will have a notable impact on Rosseland mean opacities, especially for $T > 10,000$ K. As a result, appropriate physics must be included to describe the gas at high pressure and its opacity interaction with radiation.

This study aims to increase the accessibility of Rosseland mean gas opacities in high-pressure environments across a broad temperature range from 100 K to 32,000 K. Expanding the opacities to cover a wide range of pressure and density conditions ($-8 \leq \log(R) \leq +6$) is essential for accurate modeling of substellar objects and very low-mass stars. We provide our results in a public web interface that allows users to customize the chemical mixture according to their specific research requirements. This flexibility is crucial because different research projects may focus on different chemical compositions and environmental conditions. In addition, we produce precomputed opacity tables with the inclusion of condensates, similar to P. Marigo et al. (2023).

This paper is organized as follows. Section 2 recaps the basic ingredients of the equation of state in $\mathcal{A}ESOPUS$ and $GGchem$ codes, as well as the method for calculating the Rosseland mean opacity. We additionally present some physical structures of very low-mass stars to demonstrate the need for the pressure and density ranges of the opacity tables to be expanded to higher values. Section 3 describes how we implement the IPD effect in $\mathcal{A}ESOPUS$ partition functions and abundance differential equations, as well as how we treat line pressure broadening for atomic and molecular transitions. In Section 4 we analyze and discuss the findings, focusing on the impact of the IPD effect and pressure broadening on Rosseland mean opacities and comparing our results to others found in the literature. Section 5 presents a few examples of Rosseland mean opacities with solid grains included, while Section 6 briefly discusses the impact of these opacities in low-mass stellar models.

2. Equation of State and Rosseland Mean Opacities

The $\mathcal{A}ESOPUS$ code solves the equation of state encompassing more than 800 species, including about 300 atoms and ions and 500 molecules, in the gas phase under conditions of thermodynamic and instantaneous chemical equilibrium (see Appendix). In order to expand the opacity computations in the low-temperature regime where solid grains condense, we (P. Marigo et al. 2023) recently coupled $\mathcal{A}ESOPUS$ (P. Marigo & B. Aringer 2009; P. Marigo et al. 2022) and $GGchem$ codes (P. Woitke et al. 2018). In practice, we use $\mathcal{A}ESOPUS$ for temperatures between 30,000 K and 3000 K, and then we switch to $GGchem$ for temperatures between 3000 K and 400 K. We recall that $GGchem$ computes the abundances of approximately 568 gas molecules, 55 liquid species, and nearly 200 types of solid particles.

There is an extensive description of how to calculate the Rosseland mean opacity in P. Marigo et al. (2022) and P. Marigo & B. Aringer (2009), so it will not be repeated here. To summarize, we compute the total monochromatic opacity cross section per unit mass (in $\text{cm}^2 \text{g}^{-1}$) for any chosen (ρ, T) pair by incorporating all the contributions from true absorption and scattering, for both gas and solid particles.

As previously stated in Section 1, the standard range of Rosseland mean opacities, $-8 \leq \log(R) \leq 1$, is not enough to describe the physical properties of very low-mass stars, brown dwarfs, and planets, which reach much higher densities and pressures. To demonstrate this fact, we display a few stellar structures in Figure 2 that correspond to brown dwarfs and very low-mass stars with initial masses M_i between $0.05 M_\odot$ and $0.7 M_\odot$.

Looking at the left panel of Figure 2, it is evident that a sizable portion of the structures of stars with $M_i \leq 0.7 M_\odot$ exceeds the upper limit of $\log(R) = 1$, reaching values up to $\log(R) \simeq 4$. The brown dwarf model with $M_i = 0.05 M_\odot$ extends up to $\log(R) \simeq 6$. As we will discuss in Section 6, opacity extrapolation outside of the validity range of tables may result in incorrect structural properties.

From stellar evolution theory, we know that main-sequence stars with $0.08 \lesssim M_i/M_\odot \lesssim 0.35$ are completely convective and adiabatic, regardless of the convection model used. However, convection becomes less effective for transporting energy closer to the surface, particularly in layers where hydrogen and helium are partially ionized, and the true temperature gradient, $\nabla = d \log(T)/d \log(P)$, becomes superadiabatic, that is

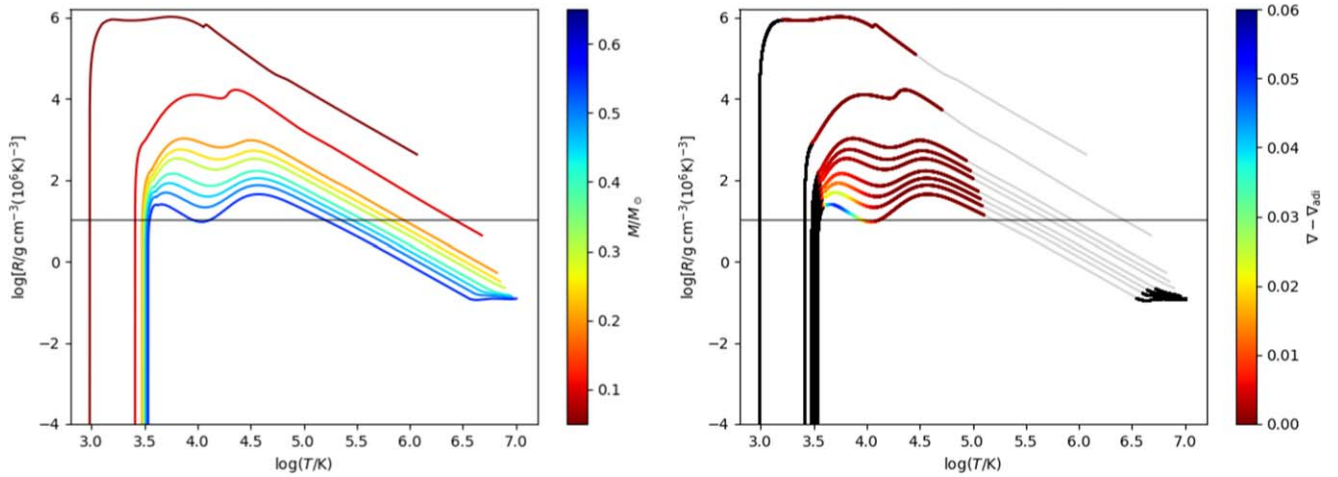


Figure 2. Structures of very low-mass stars and brown dwarfs computed with the PARSEC code (A. Bressan et al. 2012), from the center to the atmosphere, in a stage close to the zero-age main sequence. The initial mass changes in increments of $0.05 M_{\odot}$, from $0.05 M_{\odot}$ to $0.7 M_{\odot}$. The initial chemical composition is scaled solar according to E. Caffau et al. (2011), with a metallicity $Z = 0.014$, and helium abundance $Y = 0.273$. The horizontal line marks the maximum value, $\log(R) = 1$, currently available in the low-temperature Rosseland mean opacities (J. W. Ferguson et al. 2005; P. Marigo et al. 2022). Left panel: structures in the $\log(T) - \log(R)$ plane, color coded according to the initial stellar mass. Right panel: structures in the $\log(T) - \log(R)$ plane, with convective regions color coded according to the degree of superadiabaticity, $\nabla - \nabla_{\text{ad}}$. The gray sections correspond to convective regions treated as adiabatic, while the black sections refer to the radiative regions. See text for more details.

$\nabla - \nabla_{\text{ad}} > 0$. In these regions, microphysics plays a crucial role, as factors such as the equation of state and opacities become essential for determining the solution of the stellar structure. The right panel of Figure 2 highlights the regions where the temperature gradient becomes superadiabatic. The mixing-length theory (E. Böhm-Vitense 1958) is used to estimate $\nabla - \nabla_{\text{ad}}$. It is clear that in very low-mass stars, low-temperature opacities extend in stellar layers where $\log(R) > 1$ and convection is superadiabatic, and thus accurate opacity estimation is critical.

What are the chemical species that have to be considered in the calculation of Rosseland mean opacities at high values of R ? To answer this question, Figure 3 depicts the concentrations of several molecules in the gas phase as a function of temperature for $\log(R) = 6$. At high density, the most abundant molecules are molecular hydrogen (H_2) and water vapor (H_2O), carbon monoxide (CO), and silicon monoxide (SiO), followed by methane (CH_4), ammonia (NH_3), and silane (SiH_4) toward lower temperatures.

Figure 4 shows a number of condensed species, including metal oxides such as SiO, ZrO, VO, silicates, Cr, and Fe. It is worth noting that corundum (Al_2O_3) does not condense in appreciable amounts at high densities (hence, it is not shown in Figure 4). The condensation sequence at low temperatures is closed by iron sulfide (FeS), water ice (H_2O), and ammonia ice (NH_3).

3. Opacities at High Density

When entering a high-density regime, opacities become increasingly complex and must be handled with great care due to a variety of physical processes, including electron degeneracy, which increases gas pressure; nonideal effects due to Coulomb interactions among charged particles, which can lower atom and molecule ionization potentials; and line pressure broadening of molecular bands and atomic transitions. In Sections 3.1 and 3.2, we will detail the necessary improvements we made in *ÆSOPUS* to deal with these high-density conditions.

3.1. Ionization Potential Depression

The *ÆSOPUS* opacity calculations are extended up to $\log(R) = 6$ in a high-density regime. At the highest temperature, $\log(T/K) = 4.5$, this corresponds to a mass density of $\rho \simeq 32 \text{ g cm}^{-3}$. As shown in Figure 5 (left panel), electrons are partially degenerate at this density. We recall that *ÆSOPUS* incorporates an accurate treatment of electron degeneracy, based on generalized Fermi–Dirac integrals (J. Cox & R. Giuli 1968). At increasing densities, some nonideal effects appear, such as the lowering of the ionization potentials of atoms and molecules.

Let us briefly discuss this aspect. We know that the ionization potential U of an ion embedded in a plasma is reduced due to the interaction of all charged particles (ions and electrons) with that ion. The IPD effect is accounted for using the method developed by G. Ecker & W. Kröll (1963), who formulated a generalized Saha equation as a function of the chemical potential of the plasma.

The IPD is calculated with

$$\Delta U(z) = \frac{z e^2}{\lambda_D}, \quad (2)$$

where z is the charge of the ion after the ionization occurrence, e is the electron’s charge, and λ_D is a generalized Debye length, which is computed through

$$\lambda_D = \sqrt{\frac{kT}{4\pi(n_e + n_{\text{ion}})}}, \quad (3)$$

where k is the Boltzmann constant, n_e and n_{ion} are the number densities of free electron and ions in the plasma.

The implementation of the IPD effect in *ÆSOPUS* is carried out as follows. The *ÆSOPUS* code uses the Newton–Raphson technique to solve the equation of state assuming instantaneous chemical equilibrium, employing a set of dissociation–recombination and/or ionization equilibrium constants for each of the 800 particles. Concerning the Saha equation for ionization, at each iteration we correct the ionization potential

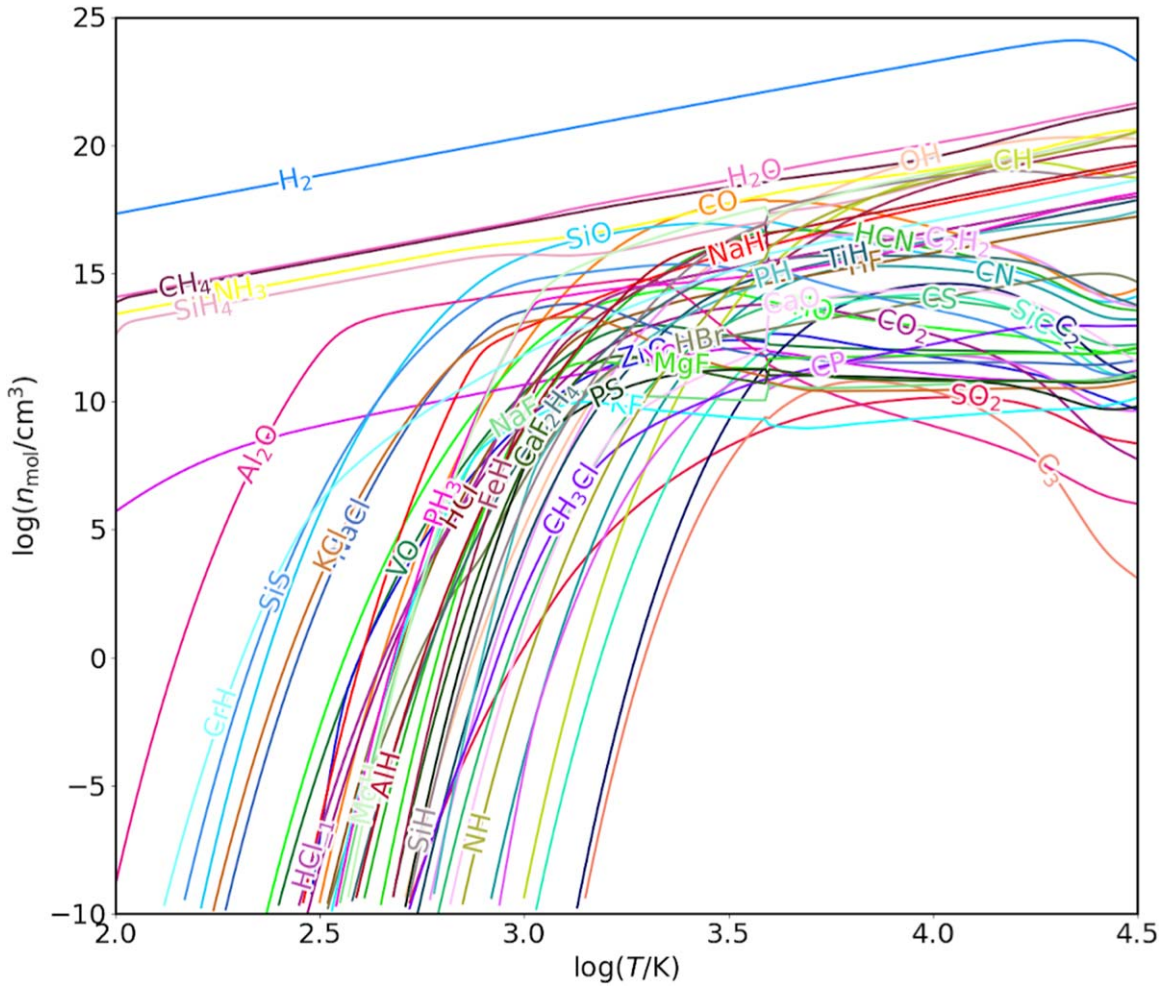


Figure 3. Gaseous molecular concentrations, in number density, for some selected species as a function of temperature, without condensation. We assume $\log(R) = 6$, with a chemical composition solar-scaled according to E. Magg et al. (2022), with metallicity $Z = 0.01$ and hydrogen abundance $X = 0.7$.

using the IPD effect inside the equilibrium constant, which depends on $U(z) - \Delta U(z)$, T , n_e , and n_{ion} until convergence is reached.

This is illustrated in the right panel of Figure 5. It compares the hydrogen ionization degree $x(\text{H})$ ⁶ with and without the IPD effect as a function of temperature for two R parameter values. Particularly for $\log(R) = 6$, with the classical Saha equation, $x(\text{H})$ remains extremely low, whereas, with the IPD plasma effect, $x(\text{H})$ increases significantly at the highest temperatures.

The locus of points in the $\log(T) - \log(\rho)$ diagram where the ionization degree for hydrogen $x(\text{H})$ is equal to 0.5 and 0.2 is plotted in Figure 5 (left panel). We observe that, when the IPD effect is considered, the same ionization degree is obtained at higher densities than in the ideal case. This is especially noticeable at the highest temperatures for $x(\text{H}) = 0.2$, while at lower densities, the differences become less and less significant.

The reduction in the ionization potential of atoms and molecules has a sizable impact on the Rosseland mean opacities at high density, as discussed in Section 4.1.

3.2. Line Pressure Broadening for Atomic and Molecular Transitions

Various processes in planet, substellar, and stellar atmospheres naturally broaden spectral lines. Doppler and pressure broadening are the most common types of line broadening. Doppler broadening is caused by the thermal velocities of each atom and molecule and is normally described by a Gaussian line profile (S. N. Yurchenko et al. 2018a). The width of the Doppler line core is directly related to the temperature. As the temperature increases, the thermal motion of particles becomes more significant, causing broader line profiles.

For instance, J. W. Ferguson et al. (2005) use a pure thermal Doppler profile in their opacity computations. In *ÆSOPUS* we do similarly but also account for microturbulence velocity by producing a normalized broadening profile, $\phi(\nu)$, according to the equation:

$$\phi(\nu) = \frac{1}{\Delta_\nu \sqrt{\pi}} e^{-\left(\frac{\nu - \nu_0}{\Delta_\nu}\right)^2}, \quad (4)$$

where ν_0 is the line center position in frequency, and Δ_ν is the line width, obtained with

$$\Delta_\nu = \frac{\nu_0}{c} \sqrt{\frac{2k_B T}{m} + \xi^2}. \quad (5)$$

⁶ The ionization degree of hydrogen is defined as the ratio $x(\text{H}) = n(\text{H}^+)/[n(\text{H}) + n(\text{H}^+)]$, where $n(\text{H})$ and $n(\text{H}^+)$ are the number densities of neutral and ionized hydrogen.

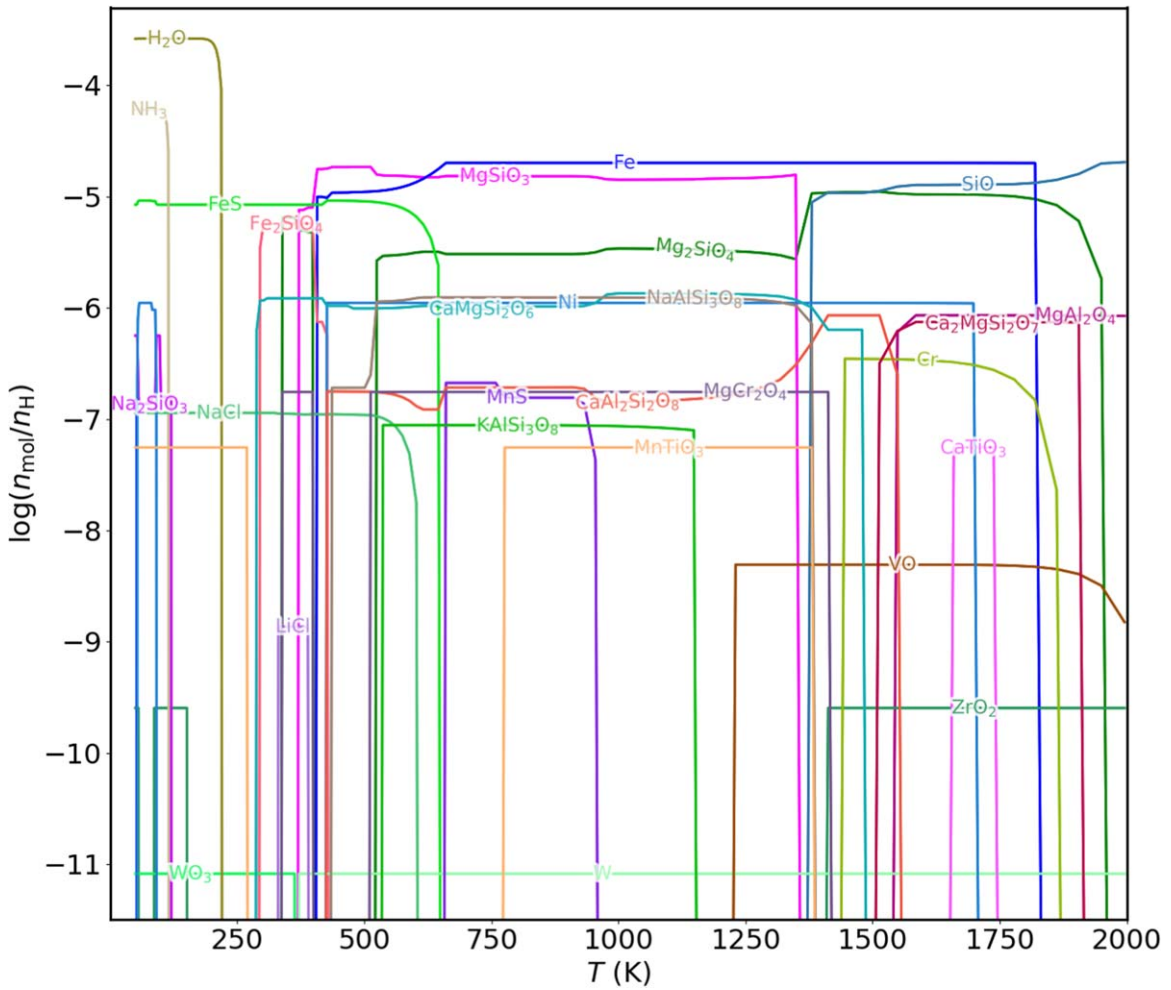


Figure 4. Distribution of several condensed species as a function of temperature at $\log(R) = 6$, for solar abundances in phase equilibrium, computed with *GGchem*. The abundances are evaluated with respect to the number density of hydrogen nuclei. The assumed $\log(R)$ value and chemical composition are the same as in Figure 4.

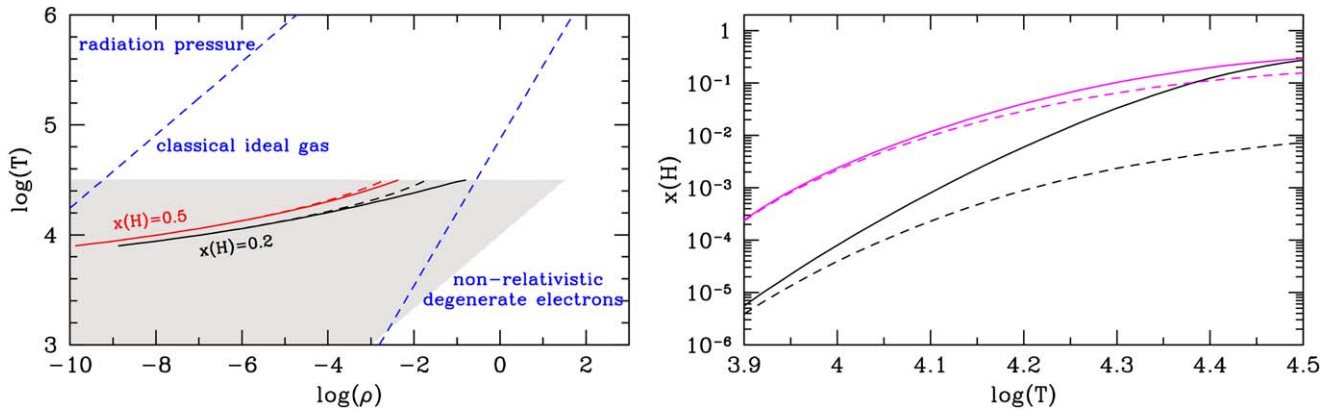


Figure 5. Left panel: the equation of state for a gas of free particles in the $\log(T) - \log(\rho)$ plane. The dashed blue lines are approximate boundaries between regions where radiation pressure, classical ideal gas pressure, and nonrelativistic electron degeneracy dominate. We assume E. Magg et al. (2022)’s solar composition with $X = 0.7$ and $Z = 0.01$. The gray area denotes the upper extension of our opacity tables. The red and black lines mark the locus of points where the ionization degree of hydrogen is 0.5 and 0.2, as indicated. Right panel: ionization degree of hydrogen as a function of temperature for $\log(R) = 6$ (black line) and $\log(R) = 3$ (magenta line). In both panels, the plasma IPD effect is represented by solid lines, while dashed lines are the result of the classical Saha ionization equation. See text for more details.

In this Equation, c denotes the speed of light, k_B the Boltzmann constant, m the molecule’s mass, and ξ the microturbulent velocity, which is set to 2.5 km s^{-1} (see P. Marigo & B. Aringer 2009; P. Marigo et al. 2022, for more details).

Pressure broadening, which varies depending on the perturbing species (such as H, He, H_2) in addition to pressure, results in a Lorentzian or Voigt profile. While a Lorentzian profile is typically pressure dependent, a Voigt profile is a

convolution of the Doppler and Lorentzian profiles. It accounts for both thermal motion and collisional broadening, making it suitable for modeling line shapes in a broader range of conditions.

In addition to temperature and pressure, the line width in Lorentzian and Voigt profiles is also influenced by various other quantities, the so-called broadening parameters, that can be challenging to determine accurately. Broadening parameters, if available, are present in the `EXOMOL` database (E. J. Barton et al. 2017; S. N. Yurchenko et al. 2017c). Based on `EXOMOL` broadening data, K. L. Chubb et al. (2021) recently created a publicly accessible database (`EXOMOLOP`⁷) of opacities for over 80 molecules of astrophysical interest computed at various pressures (10^{-5} – 10^2 bar) and temperatures (the range depends on the line list). Atomic data for the alkali-neutral metals, Na and K, is additionally provided, based on the NIST database (A. Kramida et al. 2022) and the most recent profiles for the resonance lines (N. F. Allard et al. 2016, 2019). The data can be recovered in a variety of formats that are compatible with different exoplanet atmosphere retrieval codes.

For this work we use the cross section data for the retrieval code `TauREx` (I. P. Waldmann et al. 2015a, 2015b; A. F. Al-Refaie et al. 2021), in HDF5 format, with a spectral resolution of $R = \lambda/\Delta\lambda = 15,000$, wavenumber coverage of 200 – $33,333$ cm^{-1} . The `TauREx` table format is compatible with another retrieval code `petitRADTRANS` (P. Mollière et al. 2019), so we could benefit from its publicly available software. Utilizing the `EXO k`⁸ code (J. Leconte 2021), we can create cross section tables appropriate for `ÆSOPUS` that are interpolated in pressure for each temperature value. The grids of temperature and pressure typically have 18 and 15 nodes, respectively, distributed throughout the corresponding ranges (the number of temperature nodes, as well as the wavenumber grid, may vary depending on the line list). Table 1 contains a complete list of molecules, alkali-neutral metals, and other atoms for which we have pressure-broadening line profiles. For atoms with temperatures above 4000 K, we use `Opacity Project` cross sections (M. J. Seaton et al. 1994), which are expressed as a function of temperature and electron density. Line broadening includes effects produced by thermal Doppler, radiation damping, and pressure.

The molecular data consist of 65 species, which is slightly less than the 80 species included in P. Marigo et al. (2022, see their Table 2). The molecules that currently lack pressure broadening are: O_3 , ClO , HI , CS_2 , OCS , NaO , N_2 , KOH , H_2 , HCl , ZrO , C_3 , CH_3Cl , SO . We will incorporate new data into `ÆSOPUS` as soon as it becomes available. To avoid opacity gaps, we include monochromatic cross sections for these molecules using thermal Doppler plus microturbulent velocity profiles for any (T, R) combinations. We interpolate the `TauREx` tables as a function of wavenumber, temperature, and pressure to compute monochromatic cross sections for molecules, and alkali atoms Na and K. The same procedure is applied for all molecules at T values above the T_{max} limits listed in Table 1.

It is important to know where in the pressure–temperature (P – T) space each of the two broadening mechanisms contributes most significantly. C. Hedges & N. Madhusudhan (2016) compared Doppler and Lorentzian broadening profiles

over the P – T diagram in terms of half-width at half-maximum to gain a picture of where each profile impacts substantially. Based on their findings, we depict the two broadening regimes in Figure 6. According to K. L. Chubb et al.’s (2021) analysis, we also add a lower pressure limit (10^6 bar, black line) above which molecular lines are treated with a Voigt profile. The data can be found in the `EXOMOLOP` database. As expected, thermal Doppler broadening contributes significantly to the final profile core at low pressures, whereas pressure (Lorentzian) broadening is more effective at high pressures. Both broadening mechanisms are likely to contribute considerably to the core of the line profiles closer to the border between these two regimes. In this work, we use the Voigt profile for molecular lines, which is a convolution of Lorentzian and Doppler broadening mechanisms. This convolution takes into account both pressure broadening (Lorentzian) and temperature-induced broadening (Doppler), making it a versatile tool for accurately modeling spectral lines in a variety of physical conditions. Below the black horizontal line in Figure 6 we assume that pressure effects become insignificant, and we use the thermal Doppler plus microturbulence velocity broadening.

High pressure can have a sizable impact on the monochromatic absorption cross sections σ . To illustrate the effect, Figure 7 compares σ with applied Doppler plus microturbulence broadening to pressure broadening for two molecules, water vapor (H_2O) and methane (CH_4). It is evident that pressure broadening reduces the excursion of σ to higher and lower values. In the case of water vapor, this is particularly clear at 2000 K. When compared to the thermal Doppler Gaussian profiles, the Lorentzian line profiles produce a σ that is most concentrated at higher values at a pressure of 1 bar. At 100 bar of pressure and 1000 K of temperature, methane experiences a similar effect, with a cross section that does not exhibit large fluctuations when compared to the Doppler line profiles. The tendency of σ toward higher values at increasing pressure will have a noticeable impact on Rosseland mean gas opacities, which will tend to increase.

4. Results

4.1. Ionization Potential Depression Effects

To illustrate the impact of the IPD on the opacities, we compare in Figure 8 the different contributions to the opacity for a scaled solar mixture, assuming $\log(R) = 6$. Moving up in temperature, we notice the significant contribution of collision-induced absorption (CIA) at low temperatures, which is primarily caused mainly by H_2 – H_2 collisions. The inclusion of the IPD for ions does not produce discernible effects in $\log(\kappa_{\text{R}})$, with differences < 0.02 dex up to $\log(T) = 3.75$. Beyond this temperature, the contribution of different opacity sources can vary significantly as the temperature and density increase (we assume $\log(R) = 6$). When IPD is considered, the most striking facts are: a significant decrease in H^- opacity as the number density of neutral hydrogen decreases (see right panel of Figure 5), a shift to lower temperatures of the bound-bound hydrogen line opacity, and a remarkable increase in H_2^+ opacity given its higher abundance. We also notice that at high density, metals contribute significantly to opacity in the temperature range $3.5 \lesssim \log(T/\text{K}) \lesssim 4.0$. There is a noticeable opacity bump at $3.6 \lesssim \log(T/\text{K}) \lesssim 3.7$, and we verify that the major absorption contributions come from Fe, Al, Na, and Ca. Such a bump will be visible in the Rosseland mean opacity as well (see Section 4.2).

⁷ Data is available at <https://www.exomol.com>.

⁸ https://perso.astrophy.u-bordeaux.fr/~jleconte/exo_k-doc/index.html

Table 1
Spectral Line Data for Molecular Absorption with Pressure Broadening Taken from the EXOMOL_{10P} Database

Group	Species	Line List	References	λ_l (μm)	λ_u (μm)	T_{max} (K)
Metal Oxides	AlO	ExoMol ATP	C. A. Bowesman et al. (2021)	0.29	100	8000
	CaO	ExoMol VBATHY	S. N. Yurchenko et al. (2016)	0.5	100	5000
	MgO	ExoMol LiTY	H. Y. Li et al. (2019)	0.3	100	5000
	SiO	ExoMol EBJT	S. N. Yurchenko et al. (2022)	1.65	100	9000
	TiO	ExoMol TOTO	L. K. McKemmish et al. (2019)	0.33	100	5000
	VO	ExoMol VOMYT	L. K. McKemmish et al. (2016)	0.29	100	5000
Other Oxides	CO	Li 2015	G. Li et al. (2015)	0.43	100	5000
	NO	HITEMP-2019	Q. Qu et al. (2021)	0.37	100	4000
	O ₂	HITRAN	K. L. Chubb et al. (2021)	1.43	100	296
	PO	ExoMol POPS	L. Prajapat et al. (2017)	0.83	100	5000
Triatomics	CO ₂	ExoMol UCL-4000	S. N. Yurchenko et al. (2020a)	0.5	100	4000
	H ₂ O	POKAZATEL	O. L. Polyansky et al. (2018)	0.24	100	4000
	H ₂ S	ExoMol AYT2	E. Roueff et al. (2019)	0.91	100	2000
	HCN	ExoMol Harris	G. J. Harris et al. (2006)	0.56	100	4000
	O ₃	HITRAN	I. E. Gordon et al. (2022)	1.43	100	...
	SiH ₂	ExoMol CATS	S. N. Yurchenko et al. (2017b)	1.00	100	2000
	SiO ₂	ExoMol OYT3	A. Owens et al. (2020)	1.67	100	3000
	SO ₂	ExoMol ExoAmes	K. L. Chubb et al. (2021)	1.25	100	2000
Metal hydrides	AlH	ExoMol AlHambra	S. N. Yurchenko et al. (2018d)	0.37	100	5000
	BeH	ExoMol	D. Darby-Lewis et al. (2018)	0.24	100	2000
	CaH	MoLLIST	A. Owens et al. (2022)	0.45	100	5000
	CrH	MoLLIST	P. F. Bernath (2020)	0.69	100	5000
	FeH	MoLLIST	M. C. W. Dulick et al. (2003)	0.67	100	5000
	LiH	CLT	C. M. Coppola et al. (2011)	0.5	100	2000
	MgH	MoLLIST	A. Owens et al. (2022)	0.34	100	2000
	NaH	ExoMol Rivlin	T. Rivlin et al. (2015)	0.27	100	7000
	ScH	LYT	K. L. Chubb et al. (2021)	0.63	100	2000
	TiH	MoLLIST	A. Burrows et al. (2005)	0.42	100	5000
Other hydrides	CH	MoLLIST	T. Masseron et al. (2014)	0.26	100	5000
	HBr	HITRAN	G. Li et al. (2013)	0.62	100	5000
	HCl	HITRAN	G. Li et al. (2013)	0.49	100	5000
	HF	HITRAN	G. Li et al. (2013)	0.31	100	5000
	HI	HITRAN	G. Li et al. (2013)	0.71	100	5000
	NH	MoLLIST	A. M. Fernando et al. (2018)	0.59	100	5000
	OH	MoLLIST	J. N. Hodges & P. F. Bernath (2017)	0.23	100	5000
	PH	ExoMol LaTY	J. Langleben et al. (2019)	0.41	100	4000
	SiH	ExoMol SiGHTLY	S. N. Yurchenko et al. (2017b)	0.32	100	5000
	SH	ExoMol GYT	M. N. Gorman et al. (2019)	0.26	100	5000
	Other diatomics	AlCl	MoLLIST	P. F. Bernath (2020)	4.26	100
AlF		MoLLIST	P. F. Bernath (2020)	2.58	100	5000
C ₂		ExoMol 8states	S. N. Yurchenko et al. (2018c)	0.21	100	5000
CaF		MoLLIST	S. Hou & P. F. Bernath (2018)	1.79	100	5000
CN		MoLLIST	A.-M. Syme & L. K. McKemmish (2021)	0.23	100	5000
CP		MoLLIST	Z. Qin et al. (2021)	0.67	100	5000
CS		ExoMol JnK	G. Paulose et al. (2015)	0.91	100	3000
H ₂		RACPPK	E. Roueff et al. (2019)	0.28	100	5000
KCl		ExoMol Barton	E. J. Barton et al. (2014)	3.45	100	3000
KF		MoLLIST	D. J. Frohman et al. (2016)	2.49	100	5000
LiCl		MoLLIST	D. M. Bittner & P. F. Bernath (2018)	2.07	100	5000
LiF		MoLLIST	D. M. Bittner & P. F. Bernath (2018)	5.52	100	5000
MgF		MoLLIST	S. Hou & P. F. Bernath (2017)	1.83	100	5000
NaCl		ExoMol Barton	E. J. Barton et al. (2014)	4.00	100	3000
NaF		MoLLIST	D. J. Frohman et al. (2016)	2.01	100	5000
NS		ExoMol SNaSH	S. N. Yurchenko et al. (2018b)	0.26	100	5000
PN		ExoMol YYLT	L. Yorke et al. (2014)	1.54	100	5000
PS		ExoMol POPS	L. Prajapat et al. (2017)	0.27	100	5000
SiS		ExoMol UCTY	A. Upadhyay et al. (2018)	2.70	100	5000

Table 1
(Continued)

Group	Species	Line List	References	λ_l (μm)	λ_u (μm)	T_{max} (K)
Larger molecules						
	C ₂ H ₂	ExoMol aCeTY	K. L. Chubb et al. (2020)	1.00	100	2200
	C ₂ H ₄	ExoMol MaYTY	B. P. Mant et al. (2018)	1.41	100	700
	CH ₃	ExoMol AYYJ	A. Y. Adam et al. (2019)	1.00	100	1500
	CH ₃ Cl	ExoMol OYT	A. Owens et al. (2018)	1.56	100	1200
	CH ₄	ExoMol 34to10	S. N. Yurchenko et al. (2017a)	0.56	100	2000
	NH ₃	ExoMol CoYuTe	A. R. Al Derzi et al. (2015)	0.5	100	1500
	PH ₃	ExoMol SAITY	C. Sousa-Silva et al. (2014)	1.00	100	1500
	SiH ₄	ExoMol OY2T	A. Owens et al. (2017)	2.00	100	1200
Molecular ions						
	H ₃ ⁺	ExoMol MiZATeP	I. I. Mizus et al. (2017)	0.4	100	5000
	H ₃ O ⁺	ExoMol eXeL	S. N. Yurchenko et al. (2020b)	1.00	100	1500
	HeH ⁺	ADJSAAM	P. H. R. Amaral et al. (2019)	0.67	100	4000
	LiH ⁺	CLT	C. M. Coppola et al. (2011)	10.87	100	2000
	OH ⁺	MoLLIST	J. N. Hodges & P. F. Bernath (2017)	0.33	100	5000
Alkali-neutral atoms						
	K	NIST	J. Coursey et al. (2015)	0.29	100	5000
	Na	NIST	J. Coursey et al. (2015)	5000
Other atoms						
	C N O					
	Ne Na Mg					
	Al Si S	Opacity Project	M. J. Seaton et al. (1994)	10 ⁸
	Ar Ca Cr					
	Mn Fe Ni					

Note. For each species, λ_l and λ_u denote the minimum and maximum wavelength of the corresponding line list; T_{max} is the highest temperature available.

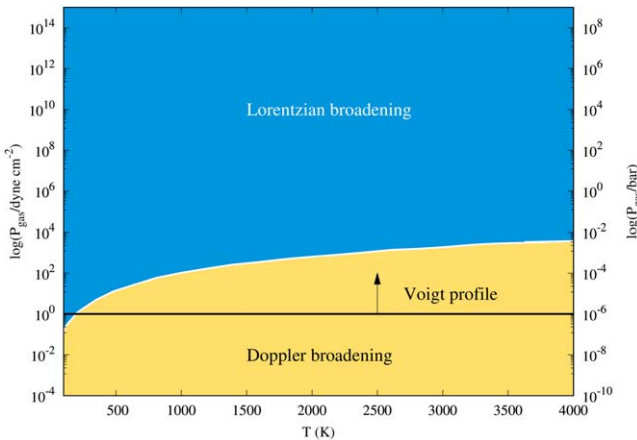


Figure 6. Comparison of the widths of Doppler line cores vs. Lorentzian profiles in the pressure–temperature diagram according to the analysis of C. Hedges & N. Madhusudhan (2016). The boundary between the two regimes is denoted by the white line. Above the horizontal black line, molecular transitions are treated with a Voigt profile extracted from the EXOMOL database (K. L. Chubb et al. 2021).

Finally, Figure 9 shows a map of the differences in $\log \kappa_R$ when the IPD effect is taken into account or neglected. The major consequence of IPD is increasing H and H₂⁺ ionization, which results in higher Rosseland mean opacity for $\log(T) > 4.1$ and $\log(R) > 1$ (red area).

4.2. Pressure-broadening Effects on Mean Gas Opacity

As thoroughly discussed in several studies (e.g., R. S. Freedman et al. 2008; C. Helling & W. Lucas 2009; M. G. Malygin et al. 2014) mean gas opacities without a dust continuum contribution

have several astrophysical applications. They are important, for example, in a dust-depleted low-metallicity medium or when the equilibrium temperature exceeds the local dust sublimation temperature. As a result, gas opacities can be relevant in describing the inner regions of accretion disks (J. Muzerolle et al. 2004), calculating the energy balance of Type Ia supernovae (L. Dessart et al. 2014), estimating the cooling of nonaccreting hot white dwarfs (R. D. Rohrmann et al. 2012), quantifying stellar feedback processes in the interstellar medium (F. I. Pelupessy & P. P. Papadopoulos 2009), and simulating star and planet formation (C. Helling & W. Lucas 2009).

To assess the impact of pressure broadening on Rosseland mean gas opacities, we performed two independent runs of *ÆSOPUS*, one adopting the thermal Doppler plus microturbulent velocity molecular line profiles, and the other assuming the Lorentzian molecular line profiles that depend on both temperature and pressure.

The results are illustrated in Figure 10. We note that the dynamical range of κ_R is extremely broad, spanning ~ 14 orders of magnitude, making eye comparison somewhat difficult. Nonetheless, we reckon it is useful to show the opacity trends in the two cases. To quantify the differences in κ_R , we create a map that spans the whole area of the table, as shown in the right panel of Figure 11. In Section 3.1, the IPD effect has already been discussed. To help the discussion, in the left panel, we also draw a map of the gas pressure, indicating the contour level (white line) above which we begin to consider pressure broadening of molecular transitions.

4.2.1. The Opacity Significance of Neutral Alkalis Na and K

The contribution of alkali atoms in atmospheric opacity of cool substellar objects was initially established by studying the

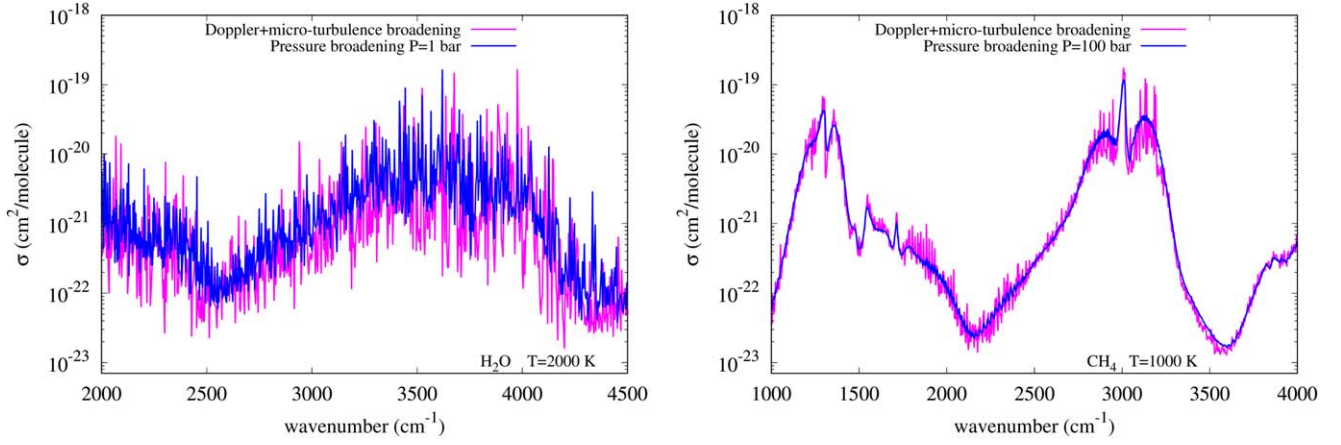


Figure 7. Comparison of two broadening profiles used for monochromatic absorption cross sections: the Lorentzian profile produced by pressure and perturbing species (blue line) and the Gaussian thermal Doppler plus microturbulent velocity profile (magenta line; see Equation (5)). Left panel: water vapor; right panel: methane. See Table 11 for details. Values for pressure and temperature are labeled.

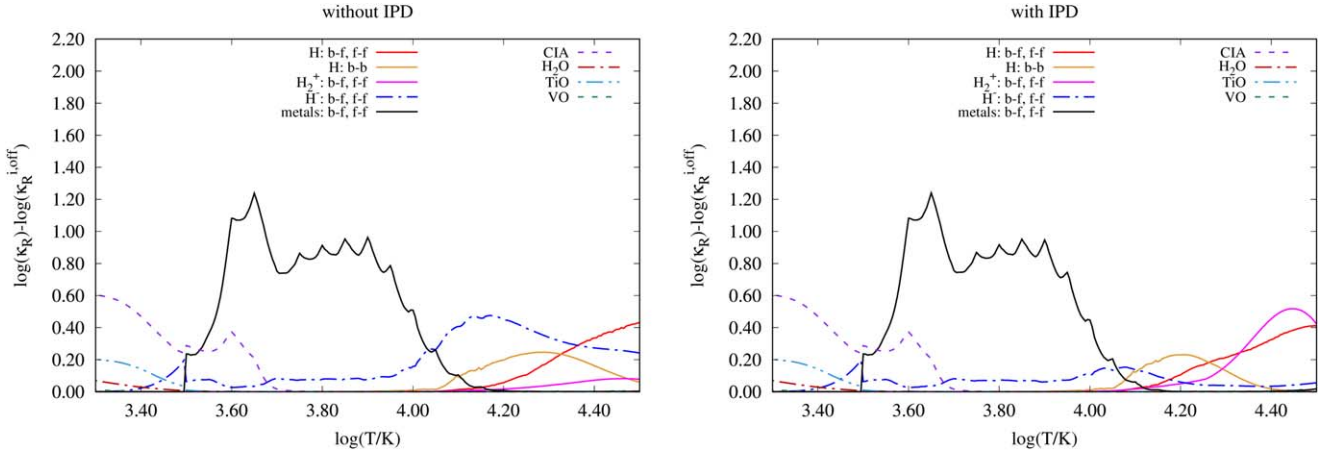


Figure 8. Properties of the Rosseland mean opacity toward the highest temperature of our tables, at high density for $\log(R) = 6$. The chemical composition is defined by $X = 0.7$, $Z = 0.01$, with a scaled solar chemical mixture following E. Magg et al. (2022). Each curve corresponds to $\log(\kappa_R) - \log(\kappa_R^{i,\text{off}})$, where κ_R is the full opacity, including all opacity sources considered here, and $\kappa_R^{i,\text{off}}$ denotes the reduced opacity obtained by excluding the specific absorbing species. This displays the temperature window to which a given opacity source contributes the most. The IPD effect is ignored in the computations of the left panel, whereas it is incorporated in the results of the right panel. In both cases, we apply thermal Doppler plus microturbulent velocity profiles for molecular transitions.

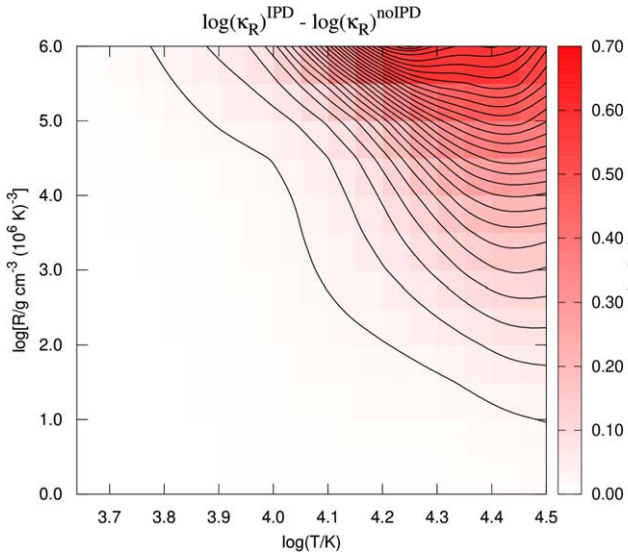


Figure 9. Map of the differences in Rosseland mean opacities when the IPD effect is included or ignored at high density. Contour levels are distributed every 0.025 dex in $\Delta \log(\kappa_R)$.

far-red spectra of T dwarfs (A. Burrows et al. 2000). Atomic pressure-broadened lines, especially those of Na and K, are major opacity sources over certain spectral ranges, temperatures, and densities (R. S. Freedman et al. 2008). With their large absorption cross sections at near-infrared and far-red wavelengths, sodium and potassium fill what would otherwise be a spectral region of relatively low opacity.

The left panel of Figure 12 compares the total molecular opacity (magenta line) as a function of wavenumber for a gas temperature of 1585 K and a gas pressure of 211 bar, with a calculation that does not account for alkali opacity (blue line). Above about a wavenumber of 10,000 cm^{-1} , the alkali opacity plays a significant role in determining the total summed opacity. The resonance Na doublet at $\approx 17,000 \text{ cm}^{-1}$ stands out as a prominent source of absorption. The right panel of Figure 12 compares the Rosseland mean opacity with and without the contribution of alkali metals at various densities. It is evident that the alkali opacity fills in the opacity minimum from about 1000 to 3200 K at higher densities. Na and K lines play a much smaller role at lower densities, so the differences are minor.

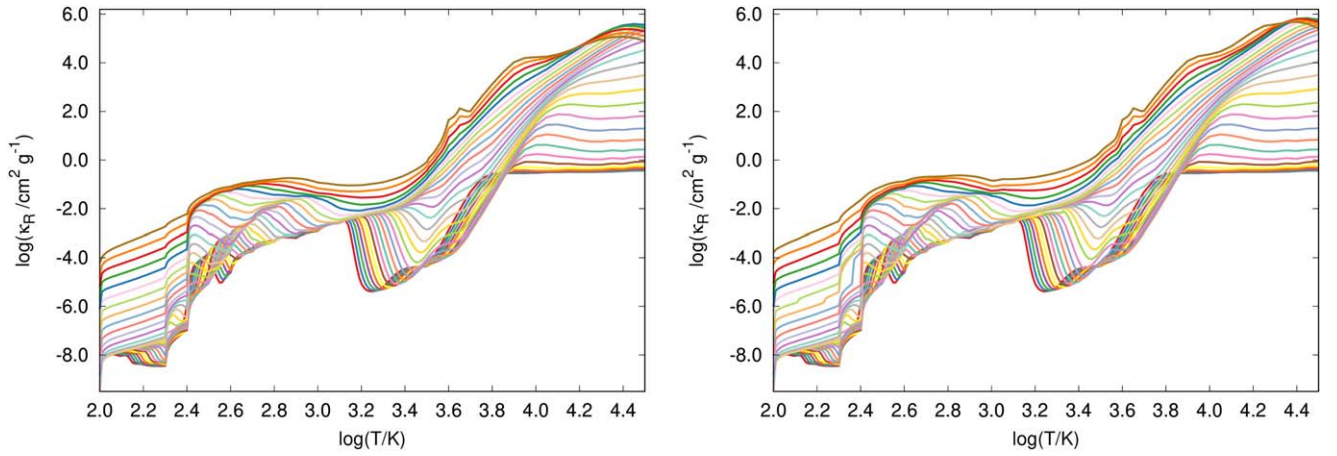


Figure 10. Rosseland mean gas opacities computed in the temperature range $100 \leq T/\text{K} \lesssim 30,000$ and encompassing the R interval $-8 \leq \log(R) \leq 6$ in steps of 0.5 dex. The chemical composition is defined by $X = 0.7$, $Z = 0.01$, with a scaled solar chemical mixture following E. Magg et al. (2022). Left panel: opacities assuming Doppler plus microturbulent velocity molecular line profiles and ignoring the IPD effect. Right panel: opacities assuming pressure broadening for molecular line profiles and accounting for the IPD effect.

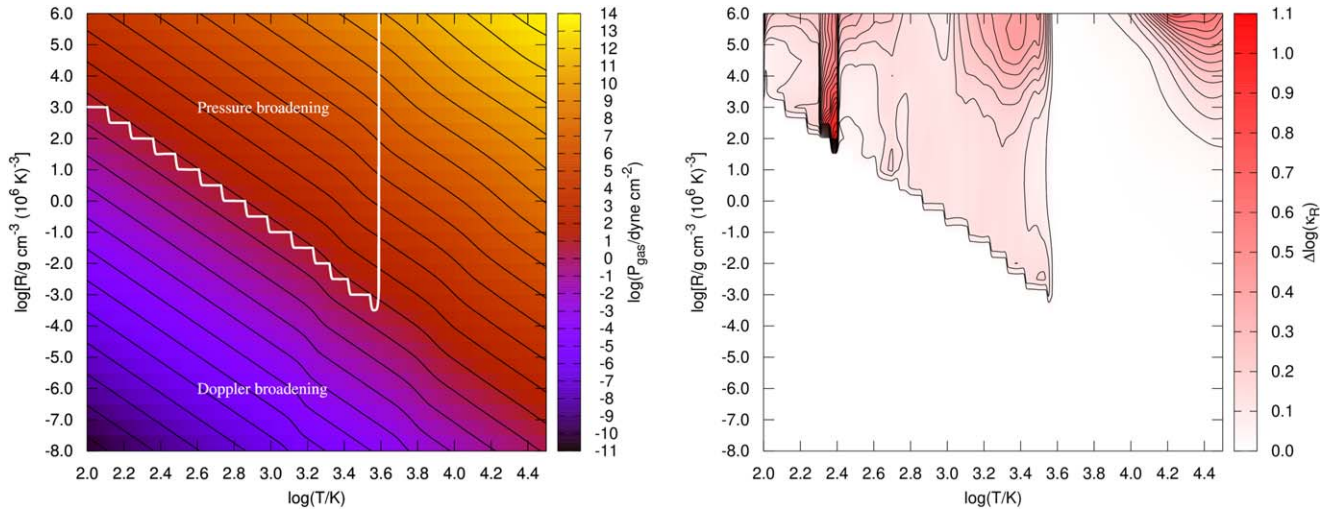


Figure 11. Left panel: map of the gas pressure as a function of T and R . Contour levels are distributed every 1 dex in $\log(P_{\text{gas}})$. The white contour draws the locus of points where the logarithmic difference in Rosseland mean opacity treated with a thermal Doppler profile and pressure broadening equals 0.001 dex in the regime where molecular transitions are important, for $T \leq 4000$ K. Right panel: map of the differences in Rosseland mean opacities between computations that include the IPD effect and pressure broadening for molecular transitions and those that ignore the IPD and assume Doppler broadening regardless of pressure. Contour levels are distributed every 0.05 dex in $\Delta \log(\kappa_R)$. The chemical composition is the same as in Figure 10.

4.2.2. Comparison with Other Authors

To test our results, we consider the Rosseland mean gas opacities computed by M. G. Malygin et al. (2014) and R. S. Freedman et al. (2014). In M. G. Malygin et al. (2014) work Kurucz’s CD-ROMs were used to extract the line and continuum opacity data (R. L. Kurucz 1993), and the mean opacities were calculated using the publicly available `DFSYNTH` code (F. Castelli 2005). The results are presented in the left panel of Figure 13 for a temperature range of 700 K–10,000 K. The agreement between the two opacity sets is good for $\log(T) > 3.6$. At lower temperatures, some deviations start to appear, most likely due to different line lists for atoms and molecules, as well as different line pressure broadening treatments. The most prominent discrepancy shows up at $\log(T) < 3.3$. While our opacity results remain either relatively flat or even increase for the highest R values, M. G. Malygin et al. (2014) opacities do, in fact, significantly decrease at lower temperatures. For example, our opacity curve for $\log(R) = -7$ only includes thermal Doppler profiles for the molecular transitions, as pressure is irrelevant in

this case. Despite this, the decrease at lower temperatures is much less pronounced than in M. G. Malygin et al. (2014). One plausible explanation is that we rely on molecular line lists that extend down to 100 K in temperature, whereas in Kurucz opacity, the contributions of molecules cease for $T < 1995$ K, and therefore extrapolations below that limit may be inaccurate.

In comparison to R. S. Freedman et al. (2014) results shown in the right panel of Figure 13, there are significant differences in Rosseland mean opacities. We found no explicit information about pressure broadening for molecular transitions, and molecular absorption is limited to 12 species. Conversely, we consider 80 absorbing molecules in our study. Both facts could explain the disparity in outcomes.

5. Rosseland Mean Opacities with Solid Grains

We present a few examples of Rosseland mean opacities with solid grains included. The dust prescriptions are the same as in P. Marigo et al. (2023). We are aware that dust clouds in brown dwarfs and planets are crucial for understanding their atmospheric

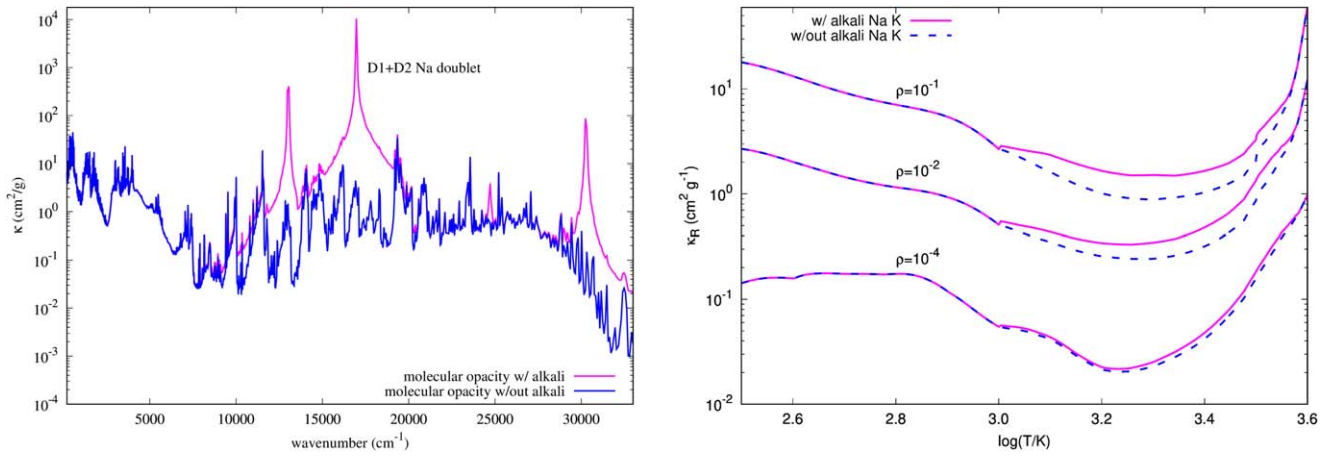


Figure 12. Left panel: molecular gas opacity as a function of wavenumber at $T = 1585$ K, gas pressure $P_{\text{gas}} = 211$ bar, and density $\rho = 0.004$ g cm $^{-3}$. The reference solar chemical composition is taken from E. Magg et al. (2022), with metallicity $Z = 0.02$ and hydrogen abundance $X = 0.7$. The blue curve represents the monochromatic opacity without the contribution of alkali atoms Na and K, whereas the magenta curve includes the two atoms' opacity contributions. Right panel: the Rosseland mean opacity as a function of temperature at three densities (g cm $^{-3}$). Magenta lines include the opacity from alkali atoms Na and K, whereas dashed blue lines do not. The chemical composition is scaled solar according to E. Magg et al. (2022), with metallicity $Z = 0.01$ and hydrogen abundance $X = 0.7$.

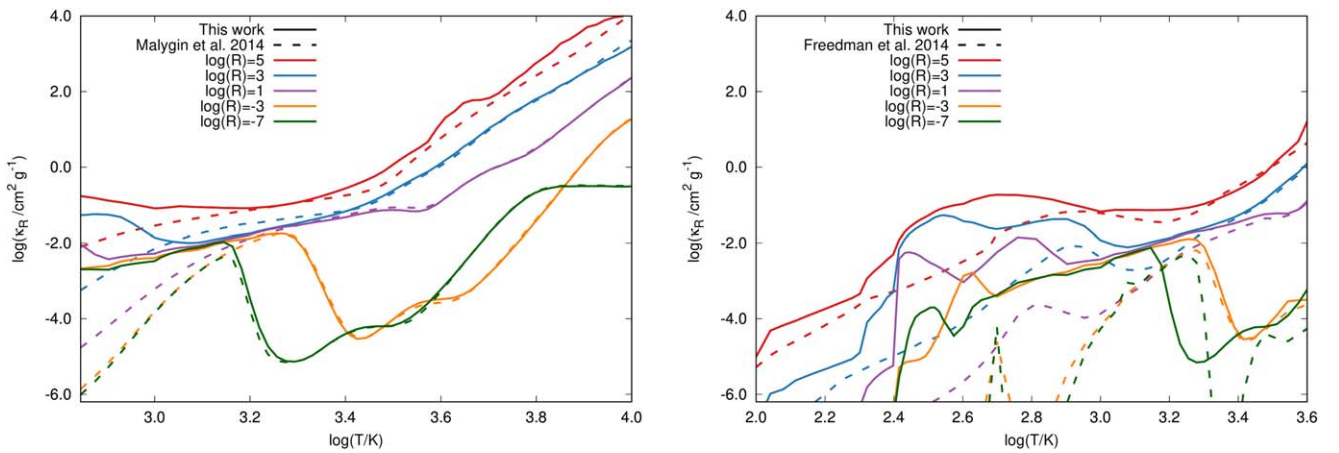


Figure 13. Comparison of Rosseland mean gas opacities computed in this work and by other studies. Left panel: Comparison with M. G. Malygin et al. (2014). The reference solar chemical composition is taken from N. Grevesse & A. J. Sauval (1998), with metallicity $Z = 0.01696$ and hydrogen abundance $X = 0.7347$. Right panel: Comparison with R. S. Freedman et al. (2014). The reference solar chemical composition is taken from K. Lodders (2003), with metallicity $Z = 0.0133$ and hydrogen abundance $X = 0.7491$. Values for $\log(R)$ are labeled.

properties, formation mechanisms, and overall behavior, providing valuable insights into the broader field of planetary science. Dust clouds can significantly impact their atmospheric composition. They often consist of various particles, including silicates, iron, and other compounds, contributing to the chemical makeup of the atmosphere. In this context, important contributions were provided by T. Tsuji et al. (1996), A. Burrows et al. (2000), A. S. Ackerman & M. S. Marley (2001), T. Tsuji (2002), C. M. Sharp & A. Burrows (2007), C. Helling et al. (2008), S. Witte et al. (2009), F. Allard et al. (2012), D. Juncher et al. (2017), P. Woitke et al. (2020). Because our primary interest is in very low-mass stars, in this work we do not take into account the formation of dust clouds, and we postpone the effort to a future study.

Figure 14 compares major solid species at low and high densities that contribute most to the opacity. There are significant differences between the two regimes.

First, we notice that the corundum opacity bump that appears for $\log(R) = -3$ at temperatures ranging from 1500 to 1200 K is missing for $\log(R) = 6$. Al_2O_3 does not condense at high-pressure conditions. Even at $\log(R) = -3$, where corundum contributes to opacity, molecular band absorption by water

molecules continues to play a significant role in opacity. This extends down to around 400 K. In contrast, for $\log(R) = 6$, the opacity contribution of water vapor is significantly reduced. Another major distinction is that at high density, solid iron is the dominant opacity source from ≈ 1870 to 650 K, whereas at lower temperatures, silicates begin to prevail. Furthermore, we see that amorphous carbon does not condense, whereas Troilite (FeS) has a discernible contribution, from about 700 to 380 K.

Figure 15 shows the behavior of Rosseland mean opacities over the range $-8 \leq \log(R) \leq 6$. As previously discussed, we see that the corundum opacity bump (at $3.08 \lesssim \log(T) \lesssim 3.17$) is present for $\log(R) < 2$, while for $\log(R) > 2$ the species does not condense and solid iron makes the most important opacity contribution for $650 \lesssim T/\text{K} \lesssim 1870$ ($2.81 \lesssim \log(T) \lesssim 3.27$).

6. Impact on Stellar Models

Figure 2 suggests that the updated Rosseland mean opacities could have a significant impact on stellar models of masses below $\sim 0.7 M_{\odot}$, particularly influencing the temperature gradient in their superadiabatic regions. This conjecture holds true, as illustrated in Figure 16, depicting the consequences of

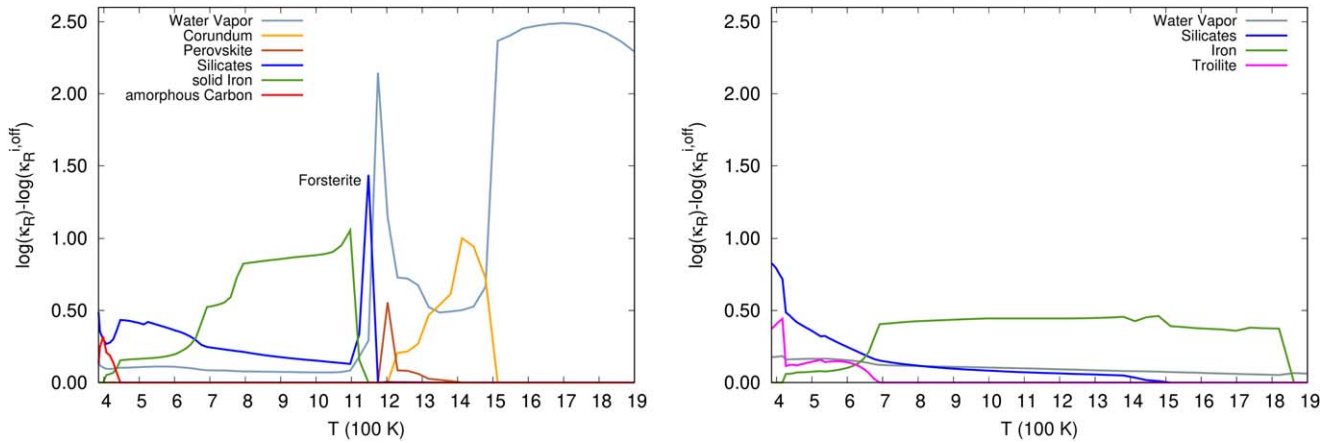


Figure 14. Properties of the Rosselland mean opacity for temperatures where solid grains dominate, at low density ($\log(R) = -3$, left panel) and high density ($\log(R) = 6$, right panel). The chemical composition is defined by $X = 0.735$, $Z = 0.0165$, with scaled solar elemental abundances following E. Magg et al. (2022). Each curve represents the contribution of major solid species to the total Rosselland mean opacity, and it is calculated as $\log(\kappa_R) - \log(\kappa_R^{i,\text{off}})$, where κ_R is the full opacity including all opacity sources considered here, and $\kappa_R^{i,\text{off}}$ is the reduced opacity computed by excluding the specific absorbing species.

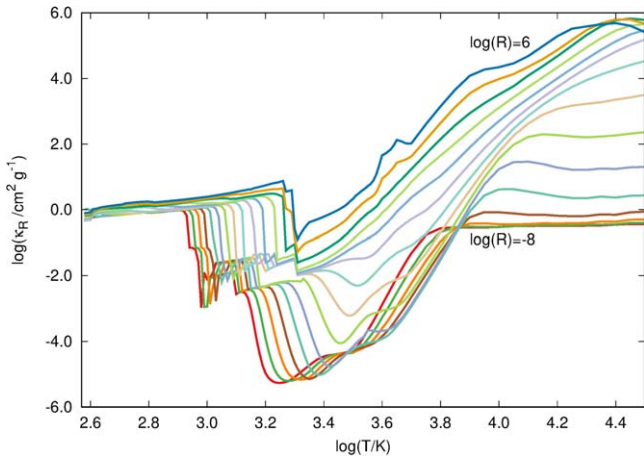


Figure 15. Rosselland mean opacities with the inclusion of condensed dust grains. The chemical composition is the same as in Figure 14. The curves are distributed every 1 dex in $\log(R)$, in the interval $-8 \leq \log(R) \leq 6$.

employing the revised opacities on the fundamental properties of PARSEC models within the mass range of 0.1 to $0.85 M_{\odot}$. These results are compared with models utilizing the prior version of $\mathcal{A}\text{ESOPUS}$ opacities (specifically, $\mathcal{A}\text{ESOPUS}$ v2.0 from P. Marigo et al. 2022). In this latter case, the opacities were not readily available for $\log(R)$ values exceeding 1, prompting PARSEC to use the opacity values taken at the border of the available tables. This assumption was grounded in the expectation that, in the extensive convective regions of such stars, the temperature gradient would approach adiabatic conditions, rendering it largely insensitive to variations in the opacity tables.

The models in Figure 16 are computed with PARSEC code version 2.0 (G. Costa et al. 2019; C. T. Nguyen et al. 2022) and adopting $T - \tau$ relations interpolated from the PHOENIX stellar atmosphere models (F. Allard et al. 2012), implemented and discussed in Y. Chen et al. (2014). Here, suffice it to recall that we use the solar composition from E. Caffau et al. (2011)⁹ and

⁹ In this case, the E. Caffau et al. (2011) composition is used in PARSEC and in the opacity tables but not in the PHOENIX atmosphere models, which are based on the M. Asplund et al. (2009) solar composition. Obtaining full consistency between all these components is beyond our reach at the moment.

the mixing-length theory with a parameter $\alpha = 1.74$ derived from the calibration of the Solar model (A. Bressan et al. 2012). We present models either using (labeled with S) or not using the shift in the $T - \tau$ relation advocated by Y. Chen et al. (2014). Further details will be discussed in a subsequent paper dedicated to very low-mass star models.

Since low-mass models evolve minimally after settling into their main sequences, only their properties at the age of 5 Gyr are presented in Figure 16. From the Hertzsprung–Russell (H–R) diagram, it is evident that the use of new opacities consistently produces cooler and fainter models. Furthermore, the impact of the new opacities diminishes as we approach stellar models with a mass of $0.6 M_{\odot}$, as expected for stellar structures that predominantly evolve in the range of $\log(R) < 1$ (refer to Figure 2).

The right panel of Figure 16 displays the same models in the mass–radius plane. In this instance, the empirical data derived from double-lined eclipsing binary catalogs is superimposed. As observed, our PARSEC models computed with $\mathcal{A}\text{ESOPUS}$ v2.0 opacities generally align with the lower limit of the empirical mass–radius relation. This once again highlights the ongoing manifestation of the mass–radius discrepancy, extensively documented in various studies (see, for example, Y. Chen et al. 2014; G. Torres et al. 2014; G. Somers et al. 2020). It is evident that the use of the new $\mathcal{A}\text{ESOPUS}$ v2.1 opacities somewhat mitigates this discrepancy by slightly inflating all models in the 0.1 – $0.6 M_{\odot}$ range. Therefore, we advocate the use of proper opacity tables extended to high densities and pressures to describe very low-mass models.

Figure 17 shows the relative differences between the observed and model radii, for the same models and data as in Figure 16, so as to allow a better visualization of the small improvements reached by using $\mathcal{A}\text{ESOPUS}$ v2.1 instead of v2.0 opacities. An additional panel presented additional models, labeled $\mathcal{A}\text{ESOPUS}$ 2.1 S, in which the $T - \tau$ relation is shifted by just half the amount calibrated in Y. Chen et al. (2014)—that is, these models adopt a shift of $\Delta \log(T/T_{\text{eff}}) = 0.03$ dex for $\log(T_{\text{eff}}/\text{K}) < 3.5$, and gradually reduce this shift to 0 for $\log(T_{\text{eff}}/\text{K})$ between 3.5 and 3.765. These latter models practically cancel out the discrepancy in the mass–radius relation at low masses.

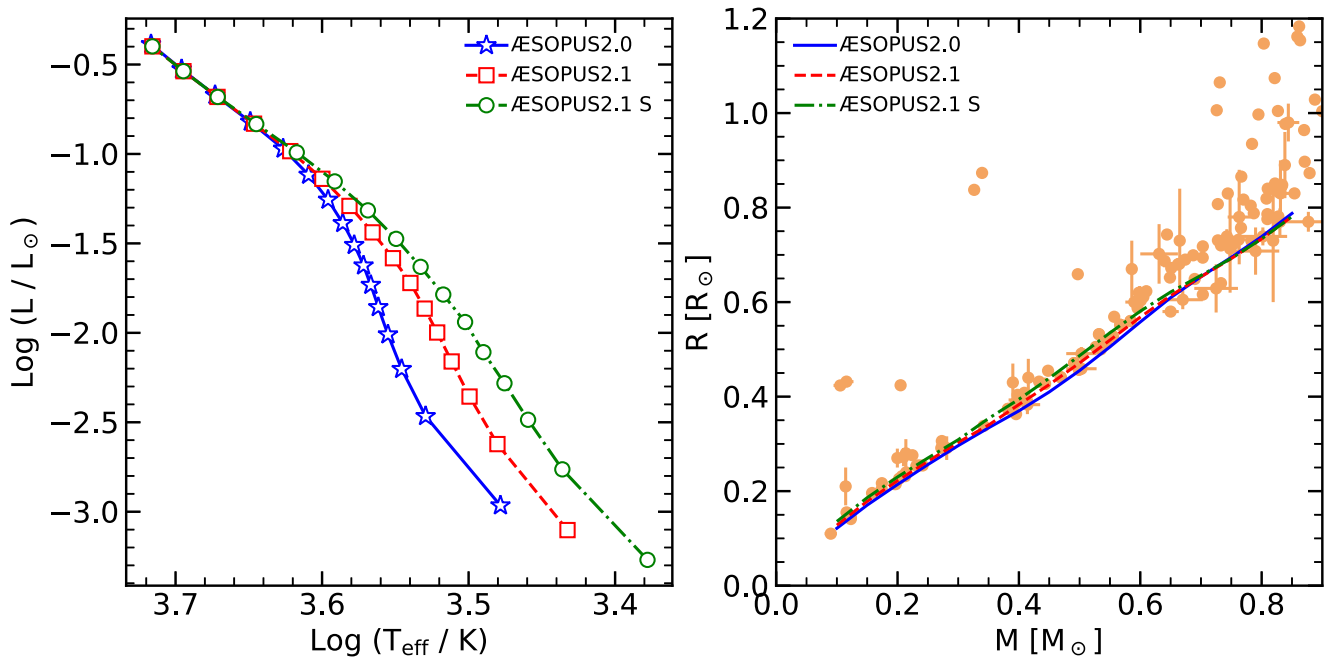


Figure 16. The impact of our new Rosseland mean opacities on low-mass stellar models computed with the PARSEC v2.0 code. The left panel shows the H-R diagram for models in the mass range from 0.1 to $0.85 M_{\odot}$ and computed at intervals of $0.05 M_{\odot}$ (from bottom right to top left) and plotted at ages of 5 Gyr. The blue symbols indicate models computed with the previous version of the opacity tables from P. Marigo et al. (2022), while the red and green symbols are for models computed with present opacity tables. The green symbols correspond to models with a shift in their $T - \tau$ relation (see text for details). The right panel shows the same models in the mass–radius plane, now compared with the empirical data of low-mass stars in double-lined eclipsing binary catalogs from D. Ségransan et al. (2003), B. O. Demory et al. (2009), G. Torres et al. (2010), J. A. Carter et al. (2011), L. R. Doyle et al. (2011), A. L. Kraus et al. (2011), S. G. Parsons et al. (2012a), S. G. Parsons et al. (2012b), J. Southworth (2015).

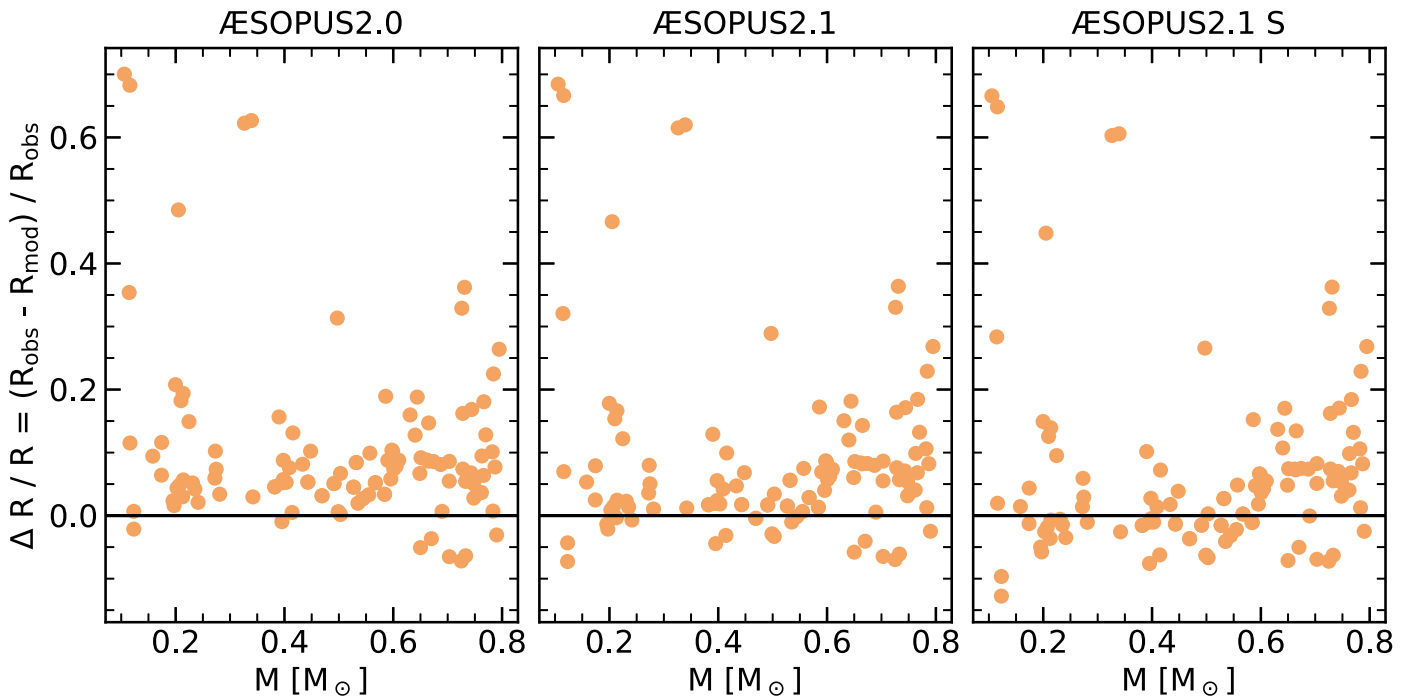


Figure 17. The relative difference between the observed and model radii for the three sets of models and the data presented in the right panel of Figure 16 as a function of stellar mass. It can be seen that while our new opacities reduce the systematic discrepancies between the predicted and observed radii for stars in the $M < 0.6 M_{\odot}$ range, a shift in the $T - \tau$ relation (or other alternatives as discussed in the text) seems to still be necessary to eliminate it completely.

Therefore, while our new $\mathcal{A}ESOPUS$ v2.1 opacities reduce the systematic discrepancies between the predicted and observed radii of very low-mass stars, additional model assumptions—

like the shift in the $T - \tau$ relation by Y. Chen et al. (2014) or the stellar spots by G. Somers et al. (2020)—seem to still be necessary to eliminate them completely.

7. Concluding Remarks

We compute the equation of state and provide Rosseland mean opacity tables for temperatures ranging from 32,000 to 100 K. These tables are expected to be useful for a series of applications, which we leave to the readers to explore. Tables for different chemical compositions can be retrieved with the updated *ÆSOPUS* web interface¹⁰ where one will also find links to a set of precomputed tables for 10 popular chemical mixtures (i.e., E. Anders & N. Grevesse 1989; N. Grevesse & A. Noels 1993; N. Grevesse & A. J. Sauval 1998; H. Holweger 2001; K. Lodders 2003; N. Grevesse et al. 2007; M. Asplund et al. 2009; E. Caffau et al. 2011; M. Asplund et al. 2021, and E. Magg et al. 2022), and in each case spanning wide ranges in Z and X values. We have so far verified that these new opacity tables lead to important changes in the modeling of very low-mass stars at near-solar metallicities, causing shifts in their mass–effective temperature and mass–luminosity relations. More modest shifts are present in the mass–radius relation, and they go in the right direction to alleviate the discrepancies in the radii of very low-mass stars that have been widely reported in the literature.

Acknowledgments

We acknowledge support from Padova University through the research project PRD 2021. P.M. and A.B. acknowledge the Italian Ministerial grant PRIN2022, “Radiative opacities for astrophysical applications,” No. 2022NEXMP8. G.C. acknowledges support from the Agence Nationale de la Recherche grant POPSYCLE No. ANR-19-CE31-0022. L.G. acknowledges partial support from an INAF Theory grant in 2022.

Software: *ÆSOPUS* (P. Marigo & B. Aringer 2009; P. Marigo et al. 2022), EXOCROSS (S. N. Yurchenko et al. 2018a), DIANA (P. Woitke et al. 2016), GGchem (P. Woitke et al. 2018).

Appendix

Chemical Species Considered in *ÆSOPUS*










For completeness, Table 2 presents the complete list of chemical species considered at the moment in the equation of state of *ÆSOPUS* 2.1.

¹⁰ The - long-lasting link for the *ÆSOPUS* 2.1 web interface is http://stev.oapd.inaf.it/cgi-bin/aesopus_2.1. We recall that the previous versions of *ÆSOPUS* are still available in their original locations at http://stev.oapd.inaf.it/cgi-bin/aesopus_1.0 and http://stev.oapd.inaf.it/cgi-bin/aesopus_2.0.

Table 2
Chemical Species Considered in the Equation of State of $\mathcal{A}\mathcal{E}\mathcal{S}\mathcal{O}\mathcal{P}\mathcal{U}\mathcal{S}$

H	H ⁺	He	He ⁺	He ⁺⁺	Li	Li ⁺	Li ⁺⁺	Be	Be ⁺	Be ⁺⁺	B	B ⁺
B ⁺⁺	C	C ⁺	C ⁺⁺	C ⁺⁺⁺	C ⁺⁺⁺⁺	N	N ⁺	N ⁺⁺	N ⁺⁺⁺	N ⁺⁺⁺⁺	O	O ⁺
O ⁺⁺	O ⁺⁺⁺	O ⁺⁺⁺⁺	O ⁺⁺⁺⁺⁺	F	F ⁺	F ⁺⁺	F ⁺⁺⁺	F ⁺⁺⁺⁺	Ne	Ne ⁺	Ne ⁺⁺	Ne ⁺⁺⁺
Ne ⁺⁺⁺⁺⁺	Ne ⁺⁺⁺⁺⁺	Na	Na ⁺	Na ⁺⁺	Na ⁺⁺⁺	Na ⁺⁺⁺⁺	Mg	Mg ⁺	Mg ⁺⁺	Mg ⁺⁺⁺	Mg ⁺⁺⁺⁺	Al
Al ⁺	Al ⁺⁺	Al ⁺⁺⁺	Al ⁺⁺⁺⁺	Si	Si ⁺	Si ⁺⁺	Si ⁺⁺⁺	Si ⁺⁺⁺⁺	P	P ⁺	P ⁺⁺	P ⁺⁺⁺
P ⁺⁺⁺⁺	S	S ⁺	S ⁺⁺	S ⁺⁺⁺	S ⁺⁺⁺⁺	Cl	Cl ⁺	Cl ⁺⁺	Cl ⁺⁺⁺	Cl ⁺⁺⁺⁺	Ar	Ar ⁺
Ar ⁺⁺	Ar ⁺⁺⁺	Ar ⁺⁺⁺⁺	K	K ⁺	K ⁺⁺	K ⁺⁺⁺	K ⁺⁺⁺⁺	Ca	Ca ⁺	Ca ⁺⁺	Ca ⁺⁺⁺	Ca ⁺⁺⁺⁺
Sc	Sc ⁺	Sc ⁺⁺	Sc ⁺⁺⁺	Sc ⁺⁺⁺⁺	Ti	Ti ⁺	Ti ⁺⁺	Ti ⁺⁺⁺	Ti ⁺⁺⁺⁺	V	V ⁺	V ⁺⁺
V ⁺⁺⁺	V ⁺⁺⁺⁺	Cr	Cr ⁺	Cr ⁺⁺	Cr ⁺⁺⁺	Cr ⁺⁺⁺⁺	Mn	Mn ⁺	Mn ⁺⁺	Mn ⁺⁺⁺	Mn ⁺⁺⁺⁺	Fe
Fe ⁺	Fe ⁺⁺	Fe ⁺⁺⁺	Fe ⁺⁺⁺⁺	Co	Co ⁺	Co ⁺⁺	Co ⁺⁺⁺	Co ⁺⁺⁺⁺	Ni	Ni ⁺	Ni ⁺⁺	Ni ⁺⁺⁺
Ni ⁺⁺⁺⁺⁺	Cu	Cu ⁺	Cu ⁺⁺	Zn	Zn ⁺	Zn ⁺⁺	Zn ⁺⁺⁺	Ga	Ga ⁺	Ga ⁺⁺	Ge	Ge ⁺
As	As ⁺	As ⁺⁺	Se	Se ⁺	Se ⁺⁺	Br	Br ⁺	Br ⁺⁺	Kr	Kr ⁺	Kr ⁺⁺	Rb
Rb ⁺	Rb ⁺⁺	Sr	Sr ⁺	Sr ⁺⁺	Y	Y ⁺	Y ⁺⁺	Zr	Zr ⁺	Zr ⁺⁺	Nb	Nb ⁺
Nb ⁺⁺	Mo	Mo ⁺	Mo ⁺⁺	Tc	Tc ⁺	Tc ⁺⁺	Ru	Ru ⁺	Ru ⁺⁺	Rh	Rh ⁺	Rh ⁺⁺
Pd	Pd ⁺	Pd ⁺⁺	Ag	Ag ⁺	Ag ⁺⁺	Cd	Cd ⁺	Cd ⁺⁺	In	In ⁺	In ⁺⁺	Sn
Sn ⁺	Sn ⁺⁺	Sb	Sb ⁺	Sb ⁺⁺	Te	Te ⁺	Te ⁺⁺	I	I ⁺	I ⁺⁺	Xe	Xe ⁺
Xe ⁺⁺	Cs	Cs ⁺	Cs ⁺⁺	Ba	Ba ⁺	Ba ⁺⁺	La	La ⁺	La ⁺⁺	Ce	Ce ⁺	Ce ⁺⁺
Pr	Pr ⁺	Pr ⁺⁺	Nd	Nd ⁺	Nd ⁺⁺	Pm	Pm ⁺	Pm ⁺⁺	Sm	Sm ⁺	Sm ⁺⁺	Eu
Eu ⁺	Eu ⁺⁺	Gd	Gd ⁺	Gd ⁺⁺	Tb	Tb ⁺	Tb ⁺⁺	Dy	Dy ⁺	Dy ⁺⁺	Ho	Ho ⁺
Ho ⁺⁺	Er	Er ⁺	Er ⁺⁺	Tm	Tm ⁺	Tm ⁺⁺	Yb	Yb ⁺	Yb ⁺⁺	Lu	Lu ⁺	Lu ⁺⁺
Hf	Hf ⁺	Hf ⁺⁺	Ta	Ta ⁺	Ta ⁺⁺	W	W ⁺	W ⁺⁺	Re	Re ⁺	Re ⁺⁺	Os
Os ⁺	Os ⁺⁺	Ir	Ir ⁺	Ir ⁺⁺	Pt	Pt ⁺	Pt ⁺⁺	Au	Au ⁺	Au ⁺⁺	Hg	Hg ⁺
Hg ⁺⁺	Tl	Tl ⁺	Tl ⁺⁺	Pb	Pb ⁺	Pb ⁺⁺	Bi	Bi ⁺	Bi ⁺⁺	Po	Po ⁺	Po ⁺⁺
At	At ⁺	At ⁺⁺	Rn	Rn ⁺	Rn ⁺⁺	Fr	Fr ⁺	Fr ⁺⁺	Ra	Ra ⁺	Ra ⁺⁺	Ac
Ac ⁺	Ac ⁺⁺	Th	Th ⁺	Th ⁺⁺	Pa	Pa ⁺	Pa ⁺⁺	U	U ⁺	U ⁺⁺	H ⁻	H ₂
H ₂ ⁺	HF	HF ⁺	HCl	HCl ⁺	HBr	HBr ⁺	HI	HeH ⁺	He ₂	He ₂ ⁺	HeNe ⁺	LiH
LiH ⁺	Li ₂	LiO	LiF	LiNa	LiCl	LiK	LiBr	LiI	BeH	BeH ⁺	BeO	BeF
BeS	BeCl	BH	BH ⁺	B ₂	BO	BF	BS	BCL	BBr	CH	CH ⁺	C ₂
C ₂ ⁺	CN	CN ⁺	CO	CO ⁺	CF	CP	CS	CS ⁺	CCl	CSe	CBR	NH
NH ⁺	N ₂	N ₂ ⁺	NO	NO ⁺	NF	NS	NS ⁺	NSe	NBr	OH	OH ⁺	O ₂
O ₂ ⁺	F ⁻	FO	F ₂	F ₂ ⁺	NeH ⁺	Ne ₂	Ne ₂ ⁺	NaH	NaO	NaF	Na ₂	Na ₂ ⁺
NaCl	NaBr	NaI	MgH	MgH ⁺	MgO	MgF	Mg ₂	MgS	MgCl	MgBr	AlH	AlO
AlF	Al ₂	AlS	AlCl	AlSe	AlBr	AlI	SiH	SiH ⁺	SiC	SiO	SiO ⁺	SiF
Si ₂	SiS	SiSe	SiTe	SiI	PH	PH ⁺	PN	PO	PO ⁺	P ₂	P ₂ ⁺	PS
SH	SH ⁺	SO	SO ⁺	SF	S ₂	S ₂ ⁺	Cl ⁻	ClO	ClF	Cl ₂	Cl ₂ ⁺	Ar ₂
KH	KO	KF	KCl	K ₂	KBr	KI	CaH	CaO	CaF	CaS	CaCl	CaCa
ScH	ScO	ScF	ScS	ScCl	TiH	TiN	TiO	TiS	VO	CrH	CrO	CrS
MnH	MnO	MnF	MnS	MnCl	FeH	FeO	CoH	CoCl	NiH	NiO	NiCl	NiBr
CuH	CuO	CuF	CuS	CuCl	Cu ₂	CuSe	CuBr	CuTe	CuI	ZnH	ZnH ⁺	ZnCl
GaH	GaO	GaF	GaCl	GaBr	GaI	GeH	GeO	GeF	GeS	GeCl	GeSe	GeTe
AsH	AsO	AsF	AsAs	SeH	SeO	SeF	SeS	Se ₂	BrO	BrF	BrCl	Br ₂
Br ₂ ⁻	KrF ⁺	RbF	RbCl	RbBr	RbI	SrH	SrO	SrF	SrS	SrCl	YO	YF
YS	ZrN	ZrO	NbO	RuC	RuO	RhC	AgH	AgO	AgF	AgAl	AgCl	AgBr
AgI	CdH	CdH ⁺	CdF	CdCl	InH	InO	InF	InCl	InBr	InI	SnH	SnO
SnF	SnS	SnSe	SnTe	SbO	SbF	SbP	SbSb	TeO	TeS	TeSe	Te ₂	IO
IF	ICl	IBr	II	Xe ₂	CsH	CsF	CsCl	CsBr	CsI	Cs ₂	BaH	BaO
BaF	BaS	BaCl	LaO	LaS	CeO	PrO	TbO	HoF	YbH	YbF	LuO	LuF
HfO	TaO	TaO ⁺	WO	IrC	IrO	PtH	PtC	PtO	AuH	Au ₂	AuSi	AuCl
Au ₂	HgH	HgH ⁺	HgF	HgCl	HgAr ⁺	TiH	TiF	TiCl	TiBr	TiI	PbH	PbO
PbF	PbS	PbCl	PbSe	PbTe	BiH	BiO	BiS	BiCl	Bi ₂	ThO	H ₂ ⁺	H ₃ ⁺
H ₂ O	H ₂ S	HBO	HBS	HCN	HCO	HCO ⁺	LiOH	BeH ₂	Be ₂ O	BeC ₂	BeOH	BeF ₂
BeClF	BeCl ₂	BH ₂	BO ₂	CH ₂	CHF	CHP	CHCl	C ₂ ⁻	C ₂ H	C ₃	C ₂ O	CN ⁻
CNC	CO ₂	COS	CS ₂	NH ₂	NO ⁻	OH ⁻	OBF	O ₃	OAlH	OAlF	OAlCl	OTiF
OTiCl	F ₂ ⁻	NaCN	NaOH	MgOH	MgF ₂	MgClF	MgCl ₂	MgBr ₂	AlOH	AlOH ⁺	AlF ₂	Al ₂ O
AlClF	AlCl ₂	SiH	SiC ₂	SiO ₂	Si ₂ C	Si ₂ N	Si ₃	PH ₂	PO ₂	SH ⁻	SO ₂	ClCN
KCN	KOH	CaOH	CaOH ⁺	CaF ₂	CaCl ₂	CaBr ₂	CaI ₂	TiO ₂	TiF ₂	TiCl ₂	TiBr ₂	TiI ₂
VO ₂	CrO ₂	FeCl ₂	FeBr ₂	BrCN	SrOH	SrOH ⁺	SrF ₂	SrCl ₂	SrBr ₂	ZrO ₂	ZrF ₂	ZrCl ₂
ZrBr ₂	ZrI ₂	NbO ₂	MoO ₂	CsOH	BaOH	BaOH ⁺	BaF ₂	BaCl ₂	BaBr ₂	TaO ₂	WO ₂	WCl ₂
H ₃ O ⁺	HBO ₂	LiBO ₂	BeBO ₂	BH ₃	BO ₂ ⁻	CH ₃	C ₂ H ₂	C ₂ HF	C ₂ HCl	C ₄	(CN) ₂	CO ₂ ⁻
NH ₃	OAlOH	OAlF ₂	NaBO ₂	(NaCl) ₂	(NaBr) ₂	AlBO ₂	AlOH ⁻	AlO ₂ ⁻	(AlO) ₂	AlF ₂ ⁻	AlCl ₂ ⁻	PH ₃
P ₄	KBO ₂	(KCl) ₂	(KBr) ₂	TiOCl ₂	TiF ₃	TiCl ₃	ZrCl ₃	MoO ₃	WO ₃	Be(OH) ₂	B(OH) ₂	CH ₄
CH ₃ Cl	C ₅	OAlF ₂ ⁻	Mg(OH) ₂	SiH ₄	SiH ₃ F	SiH ₃ Cl	SiH ₃ Br	SiH ₃ I	SiH ₂ F ₂	Ca(OH) ₂	Fe(OH) ₂	Sr(OH) ₂
ZrF ₄	ZrCl ₄	Ba(OH) ₂	WO ₂ Cl ₂	(LiOH) ₂	(BeO) ₃	C ₂ H ₄	(NaCN) ₂	(NaOH) ₂	AlF ₄ ⁻	(KOH) ₂	H ₃ BO ₃	H ₂ MoO ₄
O ₂ W(OH) ₂												

ORCID iDs

Paola Marigo  <https://orcid.org/0000-0002-9137-0773>
 Francesco Addari  <https://orcid.org/0000-0002-3867-9966>
 Diego Bossini  <https://orcid.org/0000-0002-9480-8400>
 Alessandro Bressan  <https://orcid.org/0000-0002-7922-8440>
 Guglielmo Costa  <https://orcid.org/0000-0002-6213-6988>
 Léo Girardi  <https://orcid.org/0000-0002-6301-3269>
 Giada Pastorelli  <https://orcid.org/0000-0002-9300-7409>
 Michele Trabucchi  <https://orcid.org/0000-0002-1429-2388>
 Guglielmo Volpato  <https://orcid.org/0000-0002-8691-4940>

References

- Ackerman, A. S., & Marley, M. S. 2001, *ApJ*, 556, 872
 Adam, A. Y., Yachmenev, A., Yurchenko, S. N., & Jensen, P. 2019, *JPCA*, 123, 4755
 Al Derzi, A. R., Furtenbacher, T., Tennyson, J., Yurchenko, S. N., & Csaszar, A. G. 2015, *JQSRT*, 161, 117
 Alexander, D. R. 1975, *ApJS*, 29, 363
 Alexander, D. R., & Ferguson, J. W. 1994, *ApJ*, 437, 879
 Allard, F., Homeier, D., & Freytag, B. 2012, *RSPTA*, 370, 2765
 Allard, N. F., Spiegelman, F., & Kielkopf, J. F. 2016, *A&A*, 589, A21
 Allard, N. F., Spiegelman, F., Leininger, T., & Molliere, P. 2019, *A&A*, 628, A120
 Al-Refaie, A. F., Changeat, Q., Waldmann, I. P., & Tinetti, G. 2021, *ApJ*, 917, 37
 Amaral, P. H. R., Diniz, L. G., Jones, K. A., et al. 2019, *ApJ*, 878, 95
 Anders, E., & Grevesse, N. 1989, *GeCoA*, 53, 197
 Asplund, M., Amarsi, A. M., & Grevesse, N. 2021, *A&A*, 653, A141
 Asplund, M., Grevesse, N., Sauval, A. J., & Scott, P. 2009, *ARA&A*, 47, 481
 Baraffe, I., Chabrier, G., Allard, F., & Hauschildt, P. H. 2002, *A&A*, 382, 563
 Barton, E. J., Chiu, C., Golpayegani, S., et al. 2014, *MNRAS*, 442, 1821
 Barton, E. J., Hill, C., Yurchenko, S. N., et al. 2017, *JQSRT*, 187, 453
 Bernath, P. F. 2020, *JQSRT*, 240, 106687
 Bittner, D. M., & Bernath, P. F. 2018, *ApJS*, 235, 8
 Böhm-Vitense, E. 1958, *ZAp*, 46, 108
 Bowesman, C. A., Shuai, M., Yurchenko, S. N., & Tennyson, J. 2021, *MNRAS*, 508, 3181
 Bressan, A., Marigo, P., Girardi, L., et al. 2012, *MNRAS*, 427, 127
 Burrows, A., Dulick, M., C. W. Bauschlicher, J., et al. 2005, *ApJ*, 624, 988
 Burrows, A., Hubbard, W. B., Lunine, J. I., & Liebert, J. 2001, *RvMP*, 73, 719
 Burrows, A., Marley, M. S., & Sharp, C. M. 2000, *ApJ*, 531, 438
 Caffau, E., Ludwig, H. G., Steffen, M., Freytag, B., & Bonifacio, P. 2011, *SoPh*, 268, 255
 Calamari, E., Faherty, J. K., Burningham, B., et al. 2022, *ApJ*, 940, 164
 Carter, J. A., Fabrycky, D. C., Ragozzine, D., et al. 2011, *Sci*, 331, 562
 Castellì, F. 2005, *MSAIS*, 8, 34
 Chen, Y., Girardi, L., Bressan, A., et al. 2014, *MNRAS*, 444, 2525
 Chubb, K. L., Rocchetto, M., Yurchenko, S. N., et al. 2021, *A&A*, 646, A21
 Chubb, K. L., Tennyson, J., & Yurchenko, S. N. 2020, *MNRAS*, 493, 1531
 Coppola, C. M., Lodi, L., & Tennyson, J. 2011, *MNRAS*, 415, 487
 Costa, G., Girardi, L., Bressan, A., et al. 2019, *MNRAS*, 485, 4641
 Coursey, J., Schwab, D., Tsai, J., & Dragoset, R., 2015 Atomic Weights and Isotopic Compositions v4.1, NIST, <http://physics.nist.gov/Comp>
 Cox, J., & Giuli, R. 1968, *Principles of Stellar Structure* (London: Gordon & Breach)
 Darby-Lewis, D., Tennyson, J., Lawson, K. D., et al. 2018, *JPhB*, 51, 185701
 Demory, B. O., Ségransan, D., Forveille, T., et al. 2009, *A&A*, 505, 205
 Dessart, L., Hillier, D. J., Blondin, S., & Khokhlov, A. 2014, *MNRAS*, 441, 3249
 Doyle, L. R., Carter, J. A., Fabrycky, D. C., et al. 2011, *Sci*, 333, 1602
 Dulick, M., Bauschlicher, J., Burrows, A., et al. 2003, *ApJ*, 594, 651
 Ecker, G., & Kröll, W. 1963, *PhFl*, 6, 62
 Ferguson, J. W., Alexander, D. R., Allard, F., et al. 2005, *ApJ*, 623, 585
 Fernando, A. M., Bernath, P. F., Hodges, J. N., & Masseron, T. 2018, *JQSRT*, 217, 29
 Freedman, R. S., Lustig-Yaeger, J., Fortney, J. J., et al. 2014, *ApJS*, 214, 25
 Freedman, R. S., Marley, M. S., & Lodders, K. 2008, *ApJS*, 174, 504
 Frohman, D. J., Bernath, P. F., & Brooke, J. S. 2016, *JQSRT*, 169, 104
 Gordon, I. E., Rothman, L. S., Hargreaves, R. J., et al. 2022, *JQSRT*, 277, 107949
 Gorman, M. N., Yurchenko, S. N., & Tennyson, J. 2019, *MNRAS*, 490, 1652
 Grevesse, N., Asplund, M., & Sauval, A. J. 2007, *SSRv*, 130, 105
 Grevesse, N., & Noels, A. 1993, *PhST*, 47, 133
 Grevesse, N., & Sauval, A. J. 1998, *SSRv*, 85, 161
 Hansen, J. P., & Vieillefosse, P. 1976, *PhRvL*, 37, 391
 Harris, G. J., Tennyson, J., Kaminsky, B. M., Pavlenko, Y. V., & Jones, H. R. A. 2006, *MNRAS*, 367, 400
 Hedges, C., & Madhusudhan, N. 2016, *MNRAS*, 458, 1427
 Helling, C., Ackerman, A., Allard, F., et al. 2008, *MNRAS*, 391, 1854
 Helling, C., & Lucas, W. 2009, *MNRAS*, 398, 985
 Hodges, J. N., & Bernath, P. F. 2017, *ApJ*, 840, 81
 Holweger, H. 2001, in *AIP Conf. Ser.* 598, *Solar and Galactic Composition*, ed. R. F. Wimmer-Schweingruber (Melville, NY: AIP), 23
 Hou, S., & Bernath, P. F. 2017, *JQSRT*, 203, 511
 Hou, S., & Bernath, P. F. 2018, *JQSRT*, 210, 44
 Juncher, D., Jørgensen, U. G., & Helling, C. 2017, *A&A*, 608, A70
 Kramida, D., Ralchenko, Yu., Reader, J., & NIST ASD Team, 2022 Atomic Spectra Database v5.10, NIST, <https://physics.nist.gov/asd>
 Kraus, A. L., Tucker, R. A., Thompson, M. I., Craine, E. R., & Hillenbrand, L. A. 2011, *ApJ*, 728, 48
 Kurucz, R. L. 1993, *Kurucz CD-ROM* (Cambridge, MA: Smithsonian Astrophysical Observatory)
 Langleben, J., Tennyson, J., Yurchenko, S. N., & Bernath, P. 2019, *MNRAS*, 488, 2332
 Leconte, J. 2021, *A&A*, 645, A20
 Lenzuni, P., Chernoff, D. F., & Salpeter, E. E. 1991, *ApJS*, 76, 759
 Li, G., Gordon, I. E., Hajigeorgiou, P. G., Coxon, J. A., & Rothman, L. S. 2013, *JQSRT*, 130, 284
 Li, G., Gordon, I. E., Rothman, L. S., et al. 2015, *ApJS*, 216, 15
 Li, H. Y., Tennyson, J., & Yurchenko, S. N. 2019, *MNRAS*, 486, 2351
 Lodders, K. 2003, *ApJ*, 591, 1220
 Magg, E., Bergemann, M., Serenelli, A., et al. 2022, *A&A*, 661, A140
 Malygin, M. G., Kuiper, R., Klahr, H., Dullemond, C. P., & Henning, T. 2014, *A&A*, 568, A91
 Mant, B. P., Yachmenev, A., Tennyson, J., & Yurchenko, S. N. 2018, *MNRAS*, 478, 3220
 Marigo, P., & Aringer, B. 2009, *A&A*, 508, 1539
 Marigo, P., Aringer, B., Girardi, L., & Bressan, A. 2022, *ApJ*, 940, 129
 Marigo, P., Woitke, P., Tognelli, E., et al. 2024, *ApJ*, 960, 18
 Masseron, T., Plez, B., Van Eck, S., et al. 2014, *A&A*, 571, A47
 McKemmish, L. K., Masseron, T., Hoeijmakers, H. J., et al. 2019, *MNRAS*, 488, 2836
 McKemmish, L. K., Yurchenko, S. N., & Tennyson, J. 2016, *MNRAS*, 463, 771
 Mizus, I. I., Alijah, A., Zobov, N. F., et al. 2017, *MNRAS*, 468, 1717
 Mollière, P., Wardenier, J. P., van Boekel, R., et al. 2019, *A&A*, 627, A67
 Mulders, G. D., Pascucci, I., Ciesla, F. J., & Fernandes, R. B. 2021, *ApJ*, 920, 66
 Muzerolle, J., D'Alessio, P., Calvet, N., & Hartmann, L. 2004, *ApJ*, 617, 406
 Nguyen, C. T., Costa, G., Girardi, L., et al. 2022, *A&A*, 665, A126
 Owens, A., Conway, E. K., Tennyson, J., & Yurchenko, S. N. 2020, *MNRAS*, 495, 1927
 Owens, A., Dooley, S., McLaughlin, L., et al. 2022, *MNRAS*, 511, 5448
 Owens, A., Yachmenev, A., Thiel, W., Tennyson, J., & Yurchenko, S. N. 2017, *MNRAS*, 471, 5025
 Owens, A., Yachmenev, A., Thiel, W., et al. 2018, *MNRAS*, 479, 3002
 Parsons, S. G., Marsh, T. R., Gänsicke, B. T., et al. 2012a, *MNRAS*, 419, 304
 Parsons, S. G., Marsh, T. R., Gänsicke, B. T., et al. 2012b, *MNRAS*, 420, 3281
 Paulose, G., Barton, E. J., Yurchenko, S. N., & Tennyson, J. 2015, *MNRAS*, 454, 1931
 Pelupessy, F. I., & Papadopoulos, P. P. 2009, *ApJ*, 707, 954
 Polyansky, O. L., Kyuberis, A. A., Zobov, N. F., et al. 2018, *MNRAS*, 480, 2597
 Potekhin, A. Y., Chabrier, G., Chugunov, A. I., Dewitt, H. E., & Rogers, F. J. 2009, *PhRvE*, 80, 047401
 Prajapat, L., Jagoda, P., Lodi, L., et al. 2017, *MNRAS*, 472, 3648
 Qin, Z., Bai, T., & Liu, L. 2021, *JQSRT*, 258, 107352
 Qu, Q., Yurchenko, S. N., & Tennyson, J. 2021, *MNRAS*, 504, 5768
 Rivlin, T., Lodi, L., Yurchenko, S. N., Tennyson, J., & Le Roy, R. J. 2015, *MNRAS*, 451, 634
 Rohrmann, R. D., Althaus, L. G., García-Berro, E., Córscico, A. H., & Miller Bertolami, M. M. 2012, *A&A*, 546, A119
 Rothman, L. S., Gordon, I. E., Barber, R. J., et al. 2010, *JQSRT*, 111, 2139
 Roueff, E., Abgrall, H., Czachorowski, P., et al. 2019, *A&A*, 630, A58
 Seaton, M. J., Yan, Y., Mihalas, D., & Pradhan, A. K. 1994, *MNRAS*, 266, 805
 Ségransan, D., Kervella, P., Forveille, T., & Queloz, D. 2003, *A&A*, 397, L5
 Sharp, C. M., & Burrows, A. 2007, *ApJS*, 168, 140

- Sing, D. K., Fortney, J. J., Nikolov, N., et al. 2016, *Natur*, 529, 59
- Somers, G., Cao, L., & Pinsonneault, M. H. 2020, *ApJ*, 891, 29
- Sousa-Silva, C., Al-Refaie, A. F., Tennyson, J., & Yurchenko, S. N. 2014, *MNRAS*, 446, 2337
- Southworth, J. 2015, in ASP Conf. Ser. 496, Living Together: Planets, Host Stars and Binaries, ed. S. M. Rucinski, G. Torres, & M. Zejda (San Francisco, CA: ASP), 164
- Spiegel, D. S., Burrows, A., & Milsom, J. A. 2011, *ApJ*, 727, 57
- Stewart, J. C., & Pyatt, K. D. J. 1966, *ApJ*, 144, 1203
- Syme, A.-M., & McKemmish, L. K. 2021, *MNRAS*, 505, 4383
- Tennyson, J., & Yurchenko, S. N. 2012, *MNRAS*, 425, 21
- Tennyson, J., Yurchenko, S. N., Al-Refaie, A. F., et al. 2016, *JMoSp*, 327, 73
- Torres, G., Andersen, J., & Giménez, A. 2010, *A&ARv*, 18, 67
- Torres, G., Sandberg Lacy, C. H., Pavlovski, K., et al. 2014, *ApJ*, 797, 31
- Tsuji, T. 2002, *ApJ*, 575, 264
- Tsuji, T., Ohnaka, K., & Aoki, W. 1996, *A&A*, 305, L1
- Upadhyay, A., Conway, E. K., Tennyson, J., & Yurchenko, S. N. 2018, *MNRAS*, 477, 1520
- Waldmann, I. P., Rocchetto, M., Tinetti, G., et al. 2015a, *ApJ*, 813, 13
- Waldmann, I. P., Tinetti, G., Rocchetto, M., et al. 2015b, *ApJ*, 802, 107
- Wilson, P. A., Hébrard, G., Santos, N. C., et al. 2016, *A&A*, 588, A144
- Witte, S., Helling, C., & Hauschildt, P. H. 2009, *A&A*, 506, 1367
- Woitke, P., Helling, C., & Gunn, O. 2020, *A&A*, 634, A23
- Woitke, P., Helling, C., Hunter, G. H., et al. 2018, *A&A*, 614, A1
- Woitke, P., Min, M., Pinte, C., et al. 2016, *A&A*, 586, A103
- Yorke, L., Yurchenko, S. N., Lodi, L., & Tennyson, J. 2014, *MNRAS*, 445, 1383
- Yurchenko, S. N., Al-Refaie, A. F., & Tennyson, J. 2018a, *A&A*, 614, A131
- Yurchenko, S. N., Amundsen, D. S., Tennyson, J., & Waldmann, I. P. 2017a, *A&A*, 605, A95
- Yurchenko, S. N., Blissett, A., Asari, U., et al. 2016, *MNRAS*, 456, 4524
- Yurchenko, S. N., Bond, W., Gorman, M. N., et al. 2018b, *MNRAS*, 478, 270
- Yurchenko, S. N., Mellor, T. M., Freedman, R. S., & Tennyson, J. 2020a, *MNRAS*, 496, 5282
- Yurchenko, S. N., Sinden, F., Lodi, L., et al. 2017b, *MNRAS*, 473, 5324
- Yurchenko, S. N., Szabó, I., Pyatenko, E., & Tennyson, J. 2018c, *MNRAS*, 480, 3397
- Yurchenko, S. N., Tennyson, J., & Barton, E. J. 2017c, *JPhCS*, 810, 012010
- Yurchenko, S. N., Tennyson, J., Miller, S., et al. 2020b, *MNRAS*, 497, 2340
- Yurchenko, S. N., Tennyson, J., Syme, A.-M., et al. 2022, *MNRAS*, 510, 903
- Yurchenko, S. N., Williams, H., Leyland, P. C., Lodi, L., & Tennyson, J. 2018d, *MNRAS*, 479, 1401